J. Fluid Mech. (2007), *vol.* 580, *pp.* 83–121.
doi:10.1017/S0022112007005265 Printed in the United Kingdom

Experimental and numerical studies of convection in a rapidly rotating spherical shell

N. GILLET†, D. BRITO, D. JAULT AND H.-C. NATAF

Laboratoire de Géophysique Interne et Tectonophysique, CNRS, Observatoire de Grenoble, Université Joseph–Fourier, Maison des Géosciences, BP 53, 38041 Grenoble Cedex 09, France

(Received 21 October 2005 and in revised form 28 November 2006)

Thermal convection in a rapidly rotating spherical shell is investigated experimentally and numerically. The experiments are performed in water (Prandtl number $P = 7$) and in gallium ($P = 0.025$), at Rayleigh numbers R up to 80 times the critical value in water (up to 6 times critical in gallium) and at Ekman numbers $E \sim 10^{-6}$. The measurements of fluid velocities by ultrasonic Doppler velocimetry are quantitatively compared with quasi-geostrophic numerical simulations incorporating a varying β-effect and boundary friction (Ekman pumping). In water, unsteady multiple zonal jets, weaker in amplitude than the non-axisymmetric flow, are experimentally observed and numerically reproduced at moderate forcings ($R/R_c < 40$). In this regime, zonal flows and vortices share the same length scale. Gallium experiments and strongly supercritical convection experiments in water correspond to another regime. In these turbulent flows, the zonal motion amplitude $\overline{U}$ dominates the non-axisymmetric motion amplitude $\widetilde{U}$. As a result of the reverse cascade of kinetic energy, the characteristic Rhines length scale $\ell_\beta \sim \sqrt{\overline{U}/\beta}$ of zonal jets emerges, and the boundary friction becomes the main brake on the growth of the zonal flow. A scaling law $\overline{U} \sim \widetilde{U}^{4/3}$ is then derived and verified both numerically and experimentally.

1. Introduction: the geophysical context

Paleomagnetic observations show that the Earth has possessed a global magnetic field for much of its history. Spacecraft missions have shown that other telluric or giant planets also possess a magnetic field (see Jones 2003 for a review). Observations of the Earth's magnetic field by satellites have improved considerably in the past few decades, allowing detailed analysis of its current geometry and of its recent changes (e.g. Hulot *et al.* 2002; Jackson 2003). Thermal and compositional convection inside the outer core is likely to drive the complex fluid dynamics that is the source of this magnetic field.

Numerical models of rotating spherical dynamos developed in the last decade have been shown to reproduce some of the observations, such as reversals or the dipolar geometry of the self-sustained magnetic field (see the reviews of Dormy, Valet & Courtillot 2000 and Kono & Roberts 2002). However, the extent to which these calculations model the mechanisms of generation of the Earth's magnetic field is still debated as they use unrealistic physical parameters for the rotating fluid. In particular the magnetic Prandtl number $P_m = \nu/\lambda$, the Ekman number $E = \nu/\Omega d^2$,

† Present address: Department of Earth Sciences, University of Leeds, LS2 9JT Leeds, UK.

Definition	Expression	Water experiments	Gallium experiments	Earth's core
P, Prandtl	ν/κ	7	$0.022 - 0.025$	$\sim 10^{-1}$
E, Ekman	$\nu/\Omega d^2$	$2.4 \times 10^{-6} - 9.7 \times 10^{-6}$	$9.7 \times 10^{-7} - 2.9 \times 10^{-6}$	$\sim 10^{-15}$
E_κ, thermal Ekman	$\kappa/\Omega d^2$	$3.4 \times 10^{-7} - 1.4 \times 10^{-6}$	$3.9 \times 10^{-5} - 1.2 \times 10^{-4}$	$\sim 10^{-14}$
E^*, modified Ekman	$(\kappa + \nu)/\Omega d^2$	$2.4 \times 10^{-6} - 9.7 \times 10^{-6}$	$3.9 \times 10^{-5} - 1.2 \times 10^{-4}$	$\sim 10^{-14}$
R, Rayleigh	$\alpha \Delta T \Omega^2 d^4/\kappa\nu$	$1.2 \times 10^8 - 3.3 \times 10^9$	$8.6 \times 10^6 - 8.4 \times 10^7$	–
P_m, magnetic Prandtl	ν/λ	–	1.4×10^{-6}	$\sim 10^{-6}$

TABLE 1. Values of the dimensionless parameters in the water and gallium experiments, and in the Earth's core. Numbers are calculated from the physical properties listed in table 2 (using $d = 2.3 \times 10^6$ m and $\Omega = 7.27 \times 10^{-5}$ rad s^{-1} for the Earth's core). The Rayleigh number of the Earth's core is not computed since only the superadiabatic part of ΔT is relevant.

Definition [Units]	Symbol	Water	Gallium	Earth's core
Density [kg m^{-3}]	ρ	10^3	6.1×10^3	$\sim 10^4$
Kinematic viscosity [m^2 s^{-1}]	ν	10^{-6}	$2.9 - 3.2 \times 10^{-7}$	$\sim 10^{-6}$
Thermal expansion coefficient [K^{-1}]	α	2×10^{-4}	1.3×10^{-4}	$\sim 10^{-5}$
Thermal diffusivity [m^2 s^{-1}]	κ	1.4×10^{-7}	1.3×10^{-5}	$\sim 10^{-5}$
Magnetic diffusivity [m^2 s^{-1}]	λ	–	0.21	~ 1

TABLE 2. Physical properties of liquid water, liquid gallium (Brito 1998) and their estimation for the Earth's core (De Wijs *et al.* 1998; Secco & Schloessin 1989).

and to a certain extent the thermal Prandtl number $P = \nu/\kappa$ of these simulations are not appropriate to planetary cores (ν, κ and λ are respectively the viscous, thermal and magnetic diffusivities, see tables 1 and 2; d is the width of the gap in which the fluid is enclosed and Ω is the rotation rate). The mismatch between the dimensionless numbers used in numerical models and those pertaining to planetary interiors motivates experimental studies of magnetohydrodynamics in liquid metals: in these experiments, physical properties of the liquid metal are *de facto* close to those of metallic planetary cores. The main challenge of these experiments using liquid metals is therefore to have motions rapid enough so that induction processes can counteract diffusion. This is not an easy task, as the only very recent successes in dynamo experiments (after some 50 years of unsuccessful attempts) demonstrate (Gailitis *et al.* 2000; Stieglitz & Müller 2001).

Full numerical models of magnetic field generation in planetary cores have inspired renewed attempts to derive scaling laws for the velocity and magnetic fields (Christensen & Tilgner 2004). Assuming that the flux of light elements is not carried by the thin plumes emitted from the inner core boundary, Starchenko & Jones (2002) estimated the typical velocity within the Earth's core and derived typical magnetic fields as a result. Both Starchenko & Jones (2002) and Christensen & Tilgner (2004) suggested that non-zonal velocities within core interiors scale with the energy fluxes only and do not depend directly on the magnetic field permeating these bodies. They noticed that electromagnetic stresses, on the other hand, damp the zonal flows that are commonly found in simulations of non-magnetic rotating convection.

Our work follows on from the studies of the dynamical balance (Ingersoll & Pollard 1982; Cardin & Olson 1994; Aubert *et al.* 2001) pertaining to fully developed rotating convection that have been used to build scaling laws for the planetary cores dynamics.

We present an experimental study of convection in a rapidly rotating shell – using the same set-up as Aubert *et al.* (2001) – supported by numerical simulations using the quasi-geostrophic approximation. In addition, we investigate in a companion paper (Gillet *et al.* 2007) the impact of an imposed magnetic field on the fluid flow.

Theoretical studies describe the onset of convection in a rapidly rotating thick spherical shell as a barotropic thermal Rossby wave, composed of vortices whose axes are parallel to the rotation vector $\boldsymbol{\Omega}$ (Roberts 1968; Busse 1970; Jones, Soward & Mussa 2000; note that those three papers refer to uniformly heated spheres). The critical parameters – Rayleigh number, wavenumber and frequency – are governed by a modified Ekman number $E^* = (\nu + \kappa)/\Omega d^2$ (in the theoretical studies cited above, there is no inner core, so that d would instead be the core radius). In the liquids commonly used for convective experiments (water or silicon oils, where $P \gg 1$) this number can be approximated by the Ekman number. On the other hand, in liquid metals where $P \ll 1$ the thermal Ekman number $E_\kappa = E/P$ becomes the relevant control parameter. The description of the convective motions as barotropic thermal Rossby waves has been validated in water experiments, both at low forcings (Busse & Carrigan 1976; Carrigan & Busse 1983 for the onset of convection with $E \geqslant 1.7 \times 10^{-5}$, Chamberlain & Carrigan 1986; Cordero & Busse 1992) and strong forcings (Cardin & Olson 1992 where $E \geqslant 4 \times 10^{-6}$ and R up to 50 times critical), $R = \gamma\alpha\Delta T d^4/\kappa\nu$ being the Rayleigh number with γ the gravity gradient, α the thermal expansion coefficient of the fluid and ΔT the temperature difference between the inner and the outer boundaries. Cardin & Olson (1994) – see also Sumita & Olson (2000, 2003) who used a hemispherical shell – concentrated on the evolution of the heat flux as convection develops from onset by comparing experiments performed in water with quasi-geostrophic numerical simulations. Zonal flows driven by rotating convection through Reynolds stresses have been experimentally studied by Manneville & Olson (1996) using visualization techniques.

Ultrasonic Doppler velocimetry, ideal to quantitatively measure flow velocities in liquid metals (Brito *et al.* 2001), was used by Aubert *et al.* (2001) to study nonlinear rotating convection in a sphere filled with water or gallium. They stressed the role of the inertial term in the equation of motion and proposed an inertial balance between the Coriolis, inertial and buoyancy forces in order to explain the length and velocity scales measured in the experiment. Recently, Shew & Lathrop (2005) have used a larger (and more rapidly rotating) sphere filled with liquid sodium ($P \sim 0.01$) and investigated the heat flux distribution and temperature perturbations at very low Ekman numbers. They use the critical length scale that arises at the onset of convection to interpret their temperature perturbation spectra, in which they also see the signature of a reverse cascade toward larger length scales (see below). From correlations between temperature records measured at nearby locations, they deduce the intensity of the zonal wind, that can be interpreted either as a geostrophic flow or as a thermal wind.

Starting from Gilman (1977, 1978*a*, *b*), full numerical simulations of convection in rapidly rotating spheres have been carried out to investigate some of the nonlinear processes present in such a system. For instance, the zonal wind generation was documented by Aurnou & Olson (2001) and Christensen (2001). However, these studies are for large P and at Ekman numbers $E \geqslant 3 \times 10^{-5}$, which can be deemed quite large once we take into account, for example, that there are tangential shear layers of width $E^{1/4}d$ in rapidly rotating spherical shells (Stewartson 1966). Moreover, most of these studies model free-slip boundaries that are appropriate to the atmospheric

envelopes of giant planets but not to planetary cores. Other studies have focused on the impact of the Prandtl number (Tilgner & Busse 1997) or the strength of the forcing (Christensen 2002), but still with relatively large Ekman numbers. The constraint of rotation enables the system to be reduced to two spatial coordinates. Thus detailed investigations of small-amplitude convection (Busse & Or 1986; Or & Busse 1987) used rotating annulus models with slightly inclined ends (of slope η). In these models and at low Prandtl numbers – which favours intense zonal winds – a series of bifurcations, including a transition to vacillating convection, occurs as R is increased slightly above R_c (Schnaubelt & Busse 1992; Herrmann & Busse 1997; Plaut & Busse 2002). Including a variation of η with the distance to the axis adds to the geophysical realism of the models (Chen & Zhang 2002; Plaut & Busse 2005). In the small-gap approximation, Plaut & Busse (2005) investigated the mean zonal flow driven by the Reynolds stresses and found, for $P = 7$, a retrograde zonal flow near the inner boundary and a prograde zonal flow farther from it. Chen & Zhang (2002) found, for $P = 1$, that the scale of convection is enlarged through the sequence of bifurcations that occurs before the chaotic regime. We have not been able to study weakly nonlinear convection in our experiment, which is more appropriate to fully developed convection. Morin & Dormy (2004) used a quasi-geostrophic model very similar to our numerical model (where the slope η now corresponds to a spherical boundary) to investigate the weakly nonlinear regime. They noticed that the interval of Rayleigh number in which the successive bifurcations take place shrinks as the Ekman number is decreased.

There are common features between deep rotating convection and thin-layer baroclinic convection, which has been much studied in the context of the oceanic and atmospheric dynamics. Experimental studies (e.g. Hide & Mason 1970; Read 1986; Hide, Lewis & Read 1994; Read, Lewis & Hide 1997), later coupled with numerical computations, lead to considerations of wave/vortex interaction to generate barotropic zonal winds from baroclinic eddies. Such zonally organized structures, observed both in the envelopes of giant planets and in the Earth's oceans and atmosphere, are believed to be a consequence of two-dimensional turbulence (Williams 1978; Ingersoll *et al.* 1981; Galperin *et al.* 2004). In the absence of a source and sink, the potential vorticity (sum of the relative and planetary vorticities integrated over a fluid column) tends to be mixed by the turbulent processes, and is therefore associated with zonal winds (Rhines & Young 1982; Hide & James 1983; Aubert, Jung & Swinney 2002). The two-dimensional nature of the flow leads to an inverse cascade of kinetic energy. The build-up of anisotropy, favouring flows in the azimuthal direction, has been retrieved in numerical models using the β-plane approximation. In this framework, Rhines (1975) suggested that the inverse cascade halts at the scale $\ell_\beta = \sqrt{\mathscr{U}/\beta}$, at which kinetic energy is transferred to zonal jets by Rossby wave/vortex interaction (here $\mathscr{U}$ is a measure of the typical velocity, and β is originally the northward gradient of the Coriolis frequency $f = 2\Omega$ sin(latitude)). Such a scenario has recently been validated by the experiments of Read *et al.* (2004). Whether or not the Rhines scale ℓ_β appears in such a rotating fluid flow seems to depend on how it compares with the external friction scale (Danilov & Gurarie 2002, 2004), which results from the energy balance if the interior viscous dissipation is negligible. If the external friction scale is small enough, it stops the inverse cascade and the Rhines scale cannot arise. That external friction scale had been pointed out by Manin (1990) who studied the vortex sizes as a function of the forcing in two-dimensional turbulence without the β-effect. In a coupled experimental and numerical study of differential rotation on a β-plane, Van de Konijnenberg *et al.* (1998) found that the

number of vortices was decreasing as the flow becomes more turbulent, in agreement with the scaling argument proposed by Manin (1990).

In deep convection, a quasi-geostrophic vorticity equation can also be written, where a term $\beta_{\rm dc}(s) = \Omega\, {\rm d}(\ln H)/{\rm d}s$, dependent on the variation of depth with the cylindrical radius s, replaces the β term ($H(s)$ is the half-height of a fluid column parallel to the axis of rotation; the subscript 'dc' stands for deep convection). Only the components of the velocity field orthogonal to the rotation axis are described. The quasi-geostrophic approximation requires $\mathscr{U} \ll \Omega \ell$, where ℓ is the typical equatorial length scale of the eddies. It has been used by Aubert *et al.* (2003) in a numerical simulation of the experimental results reported by Aubert *et al.* (2001). They noticed that the length scale ℓ_β based on $\beta_{\rm dc}$ is not constant throughout the container, but decreases with s since the slope of the container boundaries is larger closer to the equator. Thus, they reckoned that, in the parameter range of the experiments, there is a transition from an inner region dominated by turbulence to an outer region where Rossby waves are dominant. The radial extent of the inner region is governed by the Rhines scale ℓ_β and increases with the convective forcing. Near the equator, the slope becomes so large that Rhines' description does not apply and Rossby waves prevail. We follow the approach of Aubert, Gillet & Cardin (2003) and use the quasi-geostrophic approximation to model the experiment.

Our article follows the work of Gillet & Jones (2006), which relies on the same numerical simulations. They first give a theoretical analysis of the weakly nonlinear regime for quasi-geostrophic convection when the mean axisymmetric flow amplitude remains weak – i.e. for moderate to large Prandtl numbers. They then derive scaling laws for the velocities and temperature perturbations, that they verify up to relatively large values of the forcing (up to 50 times supercritical in Rayleigh number) at $P = 7$. In contrast to the inertial scaling (Aubert *et al.* 2001) they argue that the critical length scale ℓ_c detected at the onset of convection remains important even for very supercritical simulations. From the comparison between our experiments and our quasi-geostrophic simulations, we propose in the present paper that

(i) the approach of Gillet & Jones (2006), based on ℓ_c, holds for convection at moderate Reynolds numbers $Re = \mathscr{U} d/\nu$, in a regime where the energy $\widetilde{\mathscr{E}}$ of non-axisymmetric flow dominates the energy $\overline{\mathscr{E}}$ of the zonal flow. That regime includes convection experiments in water at $R/R_c \leqslant 40$ (see § 5.2);

(ii) at large Reynolds number the Rhines scenario holds, in a regime where $\overline{\mathscr{E}} \geqslant \widetilde{\mathscr{E}}$, but the scaling laws derived by Aubert *et al.* (2001) must be revisited: we derive the Rhines length scale from the zonal flow amplitude instead of the non-axisymmetric typical velocity. That regime includes convection experiments in gallium, as well as in water for $R/R_c > 40$ (see § 4.3 and § 5.3).

The organization of the paper is as follows. We present in § 2 the experimental apparatus and measurement techniques used in this study. We then derive in § 3 the two-dimensional quasi-geostrophic model that describes thermal convection in a rapidly rotating shell with the boundary conditions that are relevant for our experimental set-up. The onset of convection is investigated. In § 4, nonlinear convection experiments in gallium are compared to quasi-geostrophic computations. We derive scaling laws between zonal and non-zonal motions. In § 5, nonlinear convection experiments in water are compared to quasi-geostrophic computations. Finally, in § 6, results and application to planetary cores are discussed. For convenience, both cylindrical polar $(\hat{\boldsymbol{s}}, \hat{\boldsymbol{\phi}}, \hat{\boldsymbol{z}})$ and spherical coordinates $(\hat{\boldsymbol{r}}, \hat{\boldsymbol{\theta}}, \hat{\boldsymbol{\phi}})$ are used throughout the description below. To help the reader we summarize in table 3 several variables that appear in this article.

Variables	Section	Definitions
$\widetilde{U}_{\rm rad}(s)$	2.2	radial profile of the r.m.s. radial velocity
$\overline{U}_{\rm zon}(s)$	2.2	radial profile of the mean zonal velocity
$\widetilde{u}_s(s,\phi,t)$	3.2	non-axisymmetric radial velocity
$\widetilde{u}_\phi(s,\phi,t)$	3.2	non-axisymmetric azimuthal velocity
$\overline{u}_\phi(s,t)$	3.2	axisymmetric azimuthal velocity
$\widetilde{\zeta}(s,\phi,t)$	3.2	non-axisymmetric vertical vorticity
$\overline{\zeta}(s,t)$	3.2	axisymmetric vertical vorticity
$\widetilde{U}$	4.2	volumetric mean of $\widetilde{U}_{\rm rad}(s)$
$\overline{U}$	4.2	volumetric mean of $\overline{U}_{\rm zon}(s)$
$\widetilde{U}^*$	4.2	maximum of $\widetilde{U}_{\rm rad}(s)$
$\overline{U}^*$	4.2	maximum of $-\overline{U}_{\rm zon}(s)$
$\widetilde{\mathscr{E}}(t)$	4.2	volumetric mean of the non-axisymmetric kinetic energy
$\overline{\mathscr{E}}(t)$	4.2	volumetric mean of the axisymmetric kinetic energy
Re_ℓ	5.2	local Reynolds number based on the r.m.s. flow $= \widetilde{U}.\ell_c$
$\overline{Re}_\ell$	5.2	local Reynolds number based on the mean zonal flow $= \overline{U}.\ell_c$
Pe_ℓ	5.2	local Péclet number $= PRe_\ell$

TABLE 3. Definition of the variables – linked with velocities – used in this article, together with the section where they first appear.

2. The experimental set-up

2.1. *Description of the experimental apparatus*

The experimental set-up, used by Aubert *et al.* (2001) in a previous study of the rapidly rotating thermal convection, is composed of a sphere of spherical radius $r_o = 110\,\text{mm}$ through which passes a cylinder of cylindrical radius $s_i = 40\,\text{mm}$, both co-rotating around a vertical symmetry axis as seen in figure 1. The volume between the sphere and the cylinder is filled with either gallium or water; their physical properties are listed in table 2. The set-up rotates with a constant angular velocity $\Omega\,\hat{z}$, from 200 to 800 revolutions per minute (r.p.m.). The outer sphere is maintained at a constant temperature T_o during the experiments. For water experiments within a Plexiglas sphere, the control of the temperature within the shed where the experiment is installed suffices to impose isothermal boundary conditions on the outer sphere. For gallium experiments within a copper sphere, a heating resistance wound around the sphere (see figure 1*a*) is added. In this type of convective experiment with rotating containers, the centrifugal force is used as a cylindrical gravity as pioneered by Busse & Carrigan (1976); therefore, in order to drive thermal convection, the inner temperature T_i must be smaller than the outer one T_o. We regulate the inner temperature by driving a thermostated water circulation within the cylinder. From 55 mm on both sides of the equatorial plane, the inner cylinder, made of copper is covered with a thermal insulator, polyethylene HD 1000 (see figure 1*b*), so that the cylindrical radial heat flux is kept very small there. Conversely, in the centre of the sphere along the inner cylinder, temperatures are constant due to the circulation of the water in contact with the copper cylinder. The temperature difference $(T_o - T_i)$ has been varied between 8 K and 33 K. Further technical details about the experimental set-up can be found in Aubert *et al.* (2001).

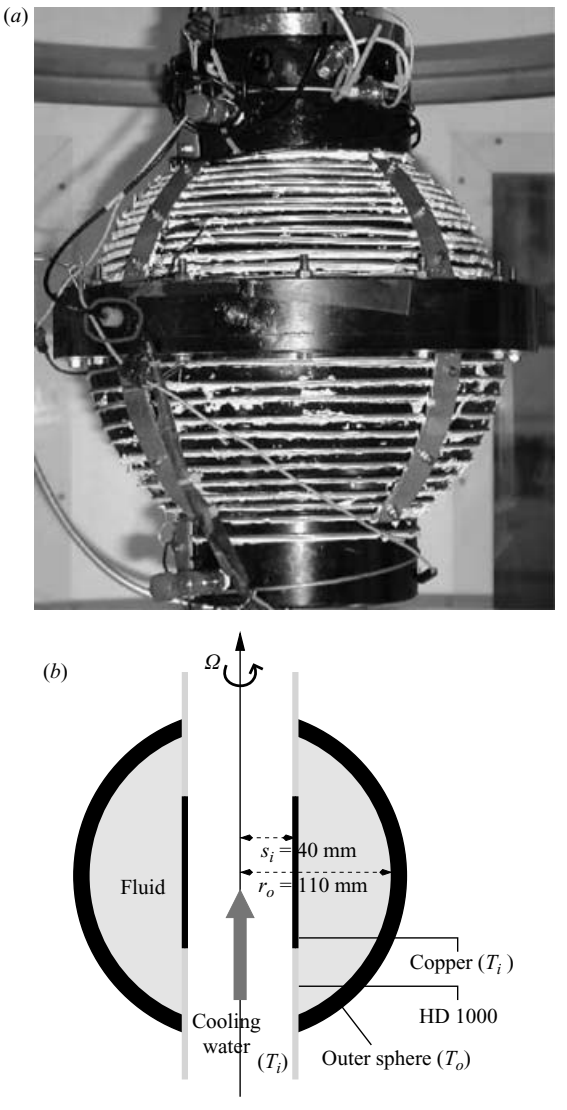

FIGURE 1. (*a*) The copper sphere used in gallium experiments. The probe used for ultrasonic Doppler velocimetry is circled at the equator. The heating resistance is wound around the sphere. (*b*) Meridional cross-section of the co-rotating sphere and inner cylinder.

2.2. *Measurement techniques*

Most previous centrifugal gravity experiments have been analysed using only visualization techniques (Cardin & Olson 1994; Manneville & Olson 1996) or temperature measurements (Sumita & Olson 2000, 2003; Shew & Lathrop 2005). We use the ultrasonic Doppler velocimetry technique here in order to measure velocities in gallium and in water (Brito *et al.* 2001; Aubert *et al.* 2001). An ultrasonic probe rotating with the sphere in the equatorial plane (see figures 1*a* and 2) emits an intermittent 4 MHz signal and receives a signal that has been sent back by particles (pollen in water experiments or gallium oxides in gallium). The signal is then analysed in the apparatus DOP2000 (model 2125, Signal Processing, Switzerland), which gives

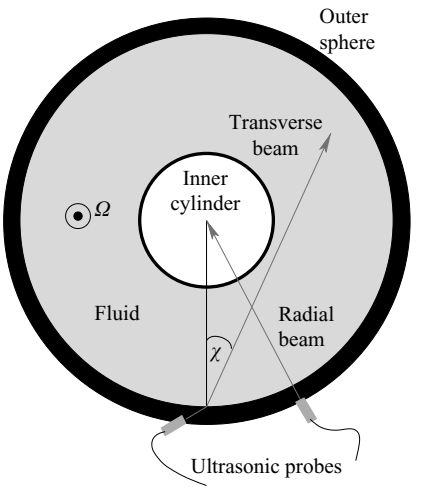

FIGURE 2. Equatorial cross-section indicating the locations of the probes and the paths followed by ultrasound beams.

the velocity profiles of the fluid along the ultrasonic beam in the equatorial plane every 160 ms in time, with a resolution down to 0.31 mm in depth. Two directions of the ultrasonic beam are used in the equatorial plane of the rotating sphere (figure 2):

(*a*) toward the axis, which gives the radial velocity field $u_s(s,t)$;

(*b*) at an angle χ with respect to the radial direction, which gives a transverse velocity field $u_\chi(s,t)$. The angle χ is $24.3^\circ \pm 1.5^\circ$ (resp. $21.5^\circ \pm 1.5^\circ$) in water experiments (resp. gallium). Thus the ultrasonic beam approaches as close as 5 ± 3 mm (resp. 1 ± 3 mm) to the inner cylinder. A more detailed explanation of the error bounds on χ can be found in Aubert *et al.* (2001, appendix A 3).

We have constructed two types of diagnostic measurements of the fluid flow:

(*a*) The radial root-mean-square (r.m.s.) velocity profile is given by

$$\widetilde{U}_{\mathrm{rad}}(s) = (\langle [u_s - \langle u_s \rangle_\tau]^2 \rangle_\tau)^{1/2},$$

where the operator $\langle \cdots \rangle_\tau = \frac{1}{\tau}\int_\tau \ldots \mathrm{d}t$. The time-average of the radial flow $\langle u_s \rangle_\tau$ (which should be zero in the case of a geostrophic flow) is the signal of the centripetal force (resp. centrifugal) acting on particles lighter (resp. denser) than the surrounding fluid. During an experiment, the average radial velocity $\langle u_s \rangle_\tau$ does not change with the integration period τ. However, $\langle u_s \rangle_\tau$ differs and even changes sign from experiment to experiment, with amplitudes up to $2\,\mathrm{mm\,s^{-1}}$. It is concentrated near the tangent cylinder (see figure 3*b*). $\langle u_s \rangle_\tau$ is assumed to be axially symmetric during an experiment.

(*b*) The mean zonal velocity profile is given by the projection of the transverse velocity profile along the azimuthal direction

$$\overline{U}_{\mathrm{zon}}(s) = \frac{s\langle u_\chi \rangle_\tau}{r_o \sin\chi}.$$

Owing to electromagnetic noise inherent to the experimental set-up, simultaneous measurements of the radial and transverse velocity profiles were not possible. We have therefore not taken into account the centripetal (or centrifugal) velocities in azimuthal velocity profiles, though one order of magnitude smaller than the mean zonal flow. Thus we have considered that the radial velocity does not alter the projection of the mean zonal flow along the transverse beam line.

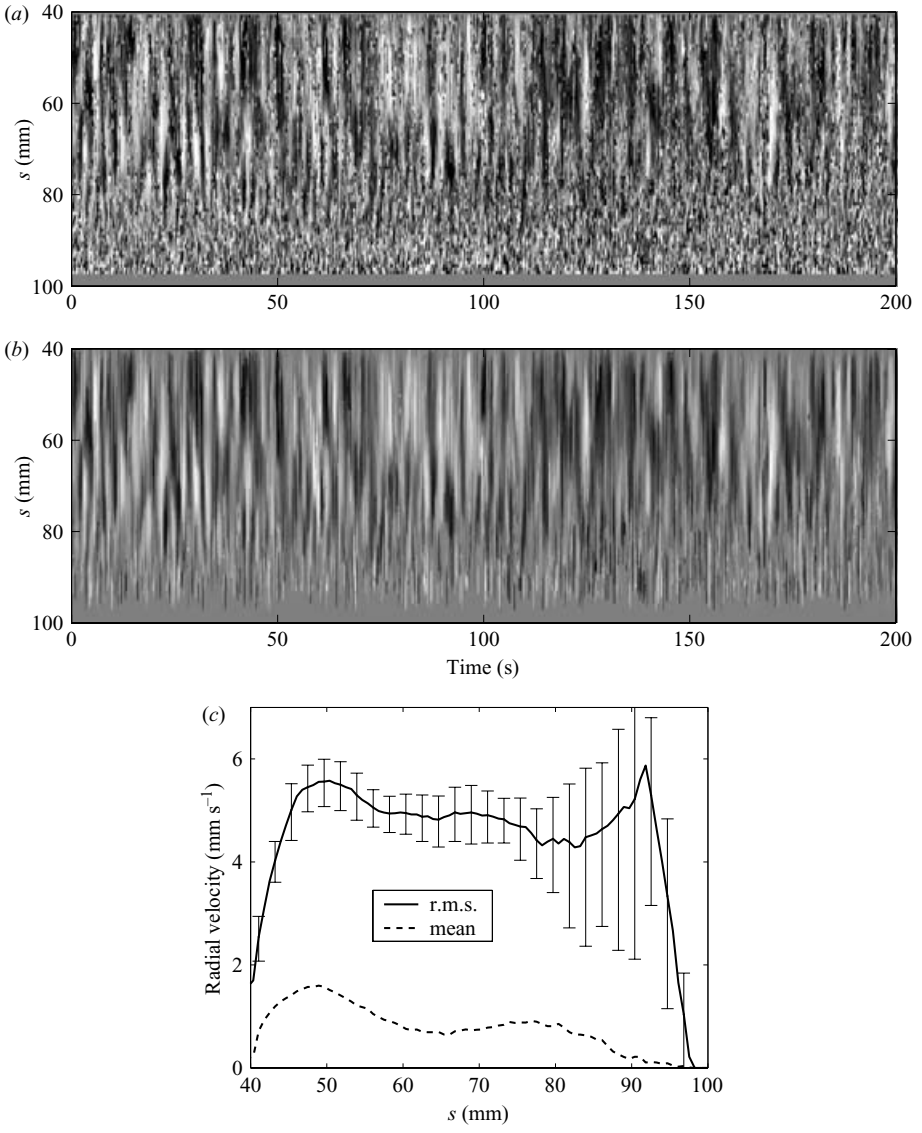

FIGURE 3. Radial velocity profiles obtained from ultrasonic Doppler velocimetry during a convection experiment performed in gallium with $\Omega = 600$ r.p.m. and $\Delta T = 19.8$ K ($E = 9.74 \times 10^{-6}$, $R = 4.3R_c$). (*a*) Measured velocity $u_s(s, t)$ as a function of time and radius. The colour scale ranges from $-12\,\mathrm{mm\,s^{-1}}$ (black) to $+12\,\mathrm{mm\,s^{-1}}$ (white). (*b*) Post-processed velocity with a 2.5 s sliding window median filter (unchanged colour scale) (*c*) R.m.s. radial velocity profile $U_{\mathrm{rad}}(s)$ and mean radial velocity $\langle u_s \rangle_{200\,s}$ extracted from the time series in (*a*). Errorbars, calculated at each radius, come from an estimate of the electromagnetic noise impact on our velocity measurement (see Gillet 2004 for more details).

Our measurements of velocity slightly differ from those of Aubert *et al.* (2001), since an improved signal processing has been used: we have benefited from a more recent apparatus and we have been able to average the signal on longer times τ (more than 10 times the typical period of the chaotic fluctuations of the fluid, e.g. from 3

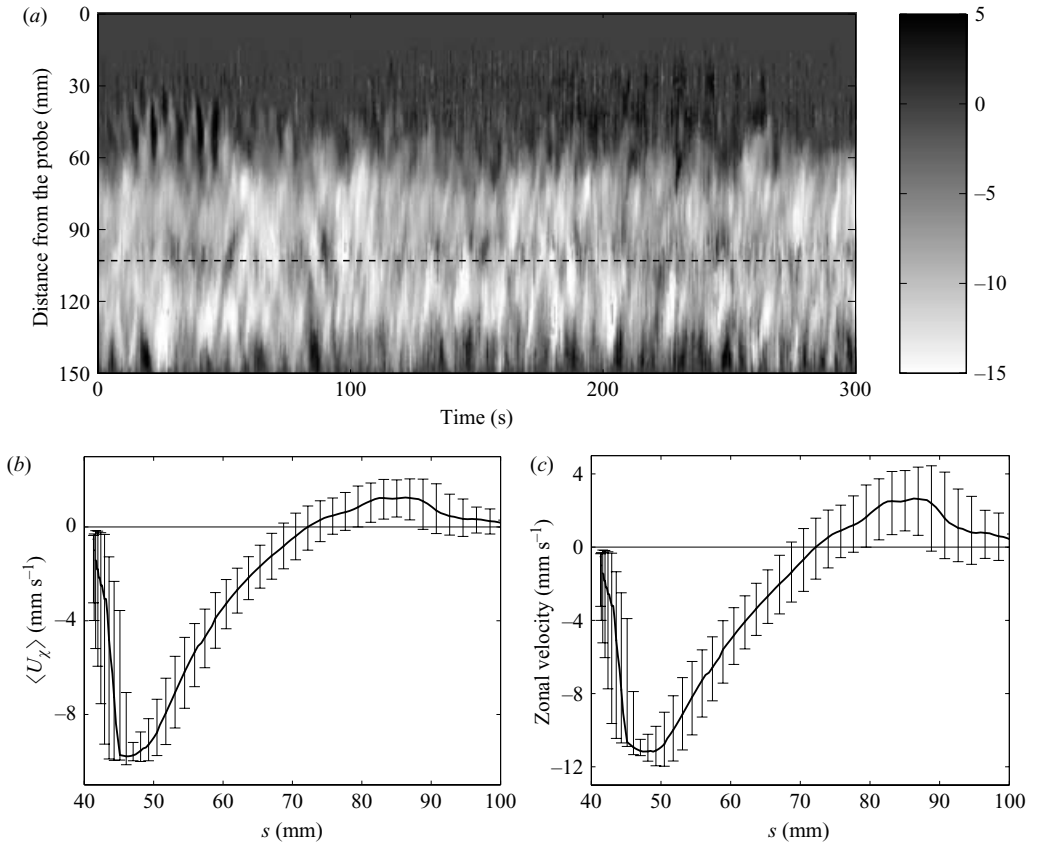

FIGURE 4. Transverse and zonal velocity profiles obtained from ultrasonic Doppler velocimetry during a convection experiment performed in gallium with $\Omega = 300$ r.p.m. and $\Delta T = 21.4$ K ($E = 1.95 \times 10^{-6}$, $R = 2.6\ R_c$). (*a*) Post-processed measured velocity $u_\chi(s,t)$, in mm s^{-1}, as a function of time and distance from the probe – post-processed with a 2.5 s sliding window median filter. The horizontal dashed line indicates the distance at which the transverse beam line is the closest to the tangent cylinder (see figure 2). (*b*) Mean transverse velocity profile $\langle u_\chi \rangle_{300\,s}$. (*c*) Mean zonal velocity profile $\overline{U}_{\rm zon}(s)$.

to 10 minutes). In order to remove electromagnetic noise, we have processed all our velocity profiles with a 15-point median filter sliding window (equivalent to 2.5 s).

The effect of that data processing on radial velocities is seen in figure 3(*b*), which shows a typical example of a radial r.m.s. velocity $\widetilde{U}_{\rm rad}(s)$ and the associated centripetal velocity, extracted from $u_s(s,t)$ in figure 3(*a*). The alternating sign of the radial velocities in figure 3(*a*) is the signature of the vortices passing the radial ultrasonic probe. The uncertainty of the measurements in our parameter regime can be lowered to around 0.1 mm s^{-1} when the signal is averaged over several periods of the chaotic fluctuations of the fluid. The amplitude of the error bars shown in figure 3 also depends on the seeding of the fluid with backscattering particles: this parameter is extremely difficult to control, in particular in the gallium experiments. More details about data processing and error bar estimates are given in Gillet (2004). Figure 4 shows typical velocity measurements obtained with the transverse probe. As will be discussed in detail in § 4 and § 5, we observe zonal jets, either steady or time varying.

In our experimental set-up, a thermal wind should arise because isodensity and isogravity surfaces are not parallel. The thermal wind should have a constant sign and should increase monotically with s. Theoretical estimates of these azimuthal velocities scale as $\alpha\Omega s\Delta T/2$ (Busse 1970); in our experiment, the intensity of that thermal wind should not exceed a few mm s^{-1}. We have found no experimental evidence for it and its theoretical amplitude is negligible compared to the mean zonal flow, which is about ten times larger.

3. Quasi-geostrophic numerical model of convection in a rapidly rotating spherical shell

3.1. *Mathematical model of the experiments*

We model thermal convection of a Boussinesq fluid between an outer sphere (spherical radius r_o) and a vertical inner cylinder (cylindrical radius s_i), the whole system rotating with a constant angular velocity $\Omega\,\hat{\boldsymbol{z}}$. In order to mimic the experiment numerically, gravity is cylindrical and increases linearly with radius as $\Omega^2 s$, so that the gravity gradient is $\gamma = \Omega^2$. We use no-slip boundary conditions for the velocity field at the boundaries. The outer sphere is at constant temperature T_o. The inner cylinder is at constant temperature T_i in its central part ($|z| \leqslant r_o/2$) and the radial heat flux vanishes ($\partial T(s_i)/\partial s = 0$) for $r_o/2 \leqslant |z| \leqslant r_o$. The continuity, momentum and heat equations in dimensionless forms are

$$\nabla \cdot \boldsymbol{u} = 0, \tag{3.1}$$

$$\frac{\mathrm{d}\boldsymbol{u}}{\mathrm{d}t} + \frac{2}{E}\hat{\boldsymbol{z}} \times \boldsymbol{u} = -\nabla \Pi - \frac{R}{P}(T - T_{\mathrm{ref}})s\hat{\boldsymbol{s}} + \nabla^2 \boldsymbol{u}, \tag{3.2}$$

$$\frac{\mathrm{d}\Theta}{\mathrm{d}t} + \boldsymbol{u} \cdot \nabla T^{\mathrm{ic}}_{\mathrm{cond}} = P^{-1}\nabla^2 \Theta, \tag{3.3}$$

where $\boldsymbol{u}$ is the velocity field, Π is the modified pressure, T is the temperature of the fluid, T_{ref} is a reference temperature, $T^{\mathrm{ic}}_{\mathrm{cond}}$ is the temperature conductive profile which satisfies the boundary conditions described above (the superscript 'ic' stands for an inner cylinder), and $\Theta = T - T^{\mathrm{ic}}_{\mathrm{cond}}$. The dimensionless numbers in the set of equations ((3.1), (3.2), (3.3)) are defined in table 1. These equations have been made non-dimensional using $\Delta T = T_o - T_i$ as the unit of temperature, the gap $d = r_o - s_i$ as the unit of length, and the viscous diffusive time d^2/ν as the unit of time. From now on in the paper r_o, s_i, T_o and T_i will be non-dimensional. Gillet & Jones (2006) have used instead the thermal diffusive time as they have derived scaling laws based on the local Péclet number. We attempt to place our study of convection in the general frame of quasi-geostrophic turbulence, which explains our choice of the viscous diffusive time.

3.2. *Quasi-geostrophic approximation of the momentum equation*

We approximate the three-dimensional model ((3.1), (3.2), (3.3)) as a quasi-geostrophic model. We assume that a geostrophic balance between the Coriolis force and the pressure gradient dominates the fluid dynamics and we take the slope η of the container boundaries as a small parameter. Denoting $H = \sqrt{r_o^2 - s^2}$ the half-height of a fluid column, we have $\eta = -\mathrm{d}H/\mathrm{d}s = s/H$.

The z-invariant geostrophic velocity field $\boldsymbol{u}^0$ is described through a stream function ψ:

$$\boldsymbol{u} = \boldsymbol{u}^0 + O(\eta) \text{ with } \boldsymbol{u}^0 = \nabla \times \hat{\boldsymbol{z}}\psi(s, \phi, t)$$

where $\boldsymbol{O}(\eta)$ represents the ageostrophic flow. Taking the z-component of the curl of the momentum equation (3.2), and averaging over z, an equation for the vertical component of the vorticity at leading order is obtained:

$$\frac{\partial \zeta^0}{\partial t} + (\boldsymbol{u}^0 \cdot \nabla)\zeta^0 - \frac{[\hat{\boldsymbol{z}} \cdot \boldsymbol{u}]_{-H}^{+H}}{EH} = \frac{R}{P}\frac{\partial}{\partial \phi}\langle \Theta \rangle_z + \nabla_H^2 \zeta^0 \tag{3.4}$$

for $s_i \leqslant s \leqslant r_0$, with

$$\zeta = \hat{\boldsymbol{z}} \cdot \nabla \times \boldsymbol{u} = \zeta^0 + O(\eta)$$

and $\zeta^0 = -\nabla_H^2 \psi(s, \phi, t)$.

$$\nabla_H^2 = \frac{1}{s}\frac{\partial}{\partial s}\left(s\frac{\partial}{\partial s}\right) + \frac{1}{s^2}\frac{\partial^2}{\partial \phi^2}$$

is the horizontal Laplacian operator (z derivatives removed),

$$\langle \cdots \rangle_z = \frac{1}{2H}\int_{-H}^{+H} \cdots \mathrm{d}z$$

is the z-average. From now on, we will remove the superscripts ^{0} for simplification. The no-slip boundary conditions are given by

$$\psi = \frac{\partial \psi}{\partial s} = 0 \text{ at } s = s_i, r_o. \tag{3.5}$$

Except for the choice of coordinate system, and the boundary conditions, our problem reduces to equation (4.1*a*) of Busse (1986). The quasi-geostrophic approximation is *a priori* valid only for $\eta \ll 1$, but we use it even though $\eta \longrightarrow \infty$ as $s \longrightarrow r_o$. The validity of this extension has previously been argued for both linear and finite-amplitude rotating convection in spherical shells (Yano 1992; Cardin & Olson 1994; Aubert *et al.* 2003; Morin & Dormy 2004).

In order to complete the quasi-geostrophic approximation of the equation of motion, we have to model the small flow induced by the Ekman layer attached to the outer sphere, and therefore model no-slip boundary conditions. Mass conservation in the Ekman layer entails flow pumping into the layer. Its component normal to the boundary can be written (Greenspan 1968)

$$\{\boldsymbol{u} \cdot \boldsymbol{n}\}_{|\pm H} = -\frac{E^{1/2}}{2}\boldsymbol{n} \cdot \nabla \times \left[\frac{\boldsymbol{n} \times \boldsymbol{u}^b \pm \boldsymbol{u}^b}{\sqrt{\boldsymbol{n} \cdot \boldsymbol{e}_z}}\right], \tag{3.6}$$

where $\boldsymbol{u}^b$ is the velocity in the fluid interior, and $\boldsymbol{n}$ is the outward unit vector normal to the boundary. Thus, we obtain

$$\pm u_{z|\pm H} = \frac{r_o}{H}\{\boldsymbol{u} \cdot \boldsymbol{n}\}_{|\pm H} - \eta u_s. \tag{3.7}$$

Substituting the expressions (3.7) and (3.6) in (3.4) gives (Schaeffer & Cardin 2005)

with

$$\left.\begin{aligned} &\frac{\partial \zeta}{\partial t} + (\boldsymbol{u} \cdot \nabla)\,\zeta + \beta u_s = \frac{R}{P}\frac{\partial}{\partial \phi}\,\langle \Theta \rangle_z + \nabla_H^2 \zeta + E^{-1/2}\Phi(\boldsymbol{u}) \\ &\Phi(\boldsymbol{u}) = -\left(\frac{r_o}{H}\right)^{3/2}\left[\zeta + \frac{s}{2H^2}u_\phi - \frac{s}{H^2}\frac{\partial u_s}{\partial \phi} + \frac{5}{2}\frac{r_o s}{H^3}u_s\right]. \end{aligned}\right\} \tag{3.8}$$

The parameter β, given here in its dimensionless form

$$\beta(s) = \frac{2\eta}{EH} = \frac{2s}{EH^2}, \tag{3.9}$$

is equivalent to the latitudinal variation of the Coriolis parameter that enters the β-plane equations for flows in a shallow-layer system. The description of the motions through the vorticity equation (3.8) is defined up to an arbitrary gradient function, which corresponds to axially symmetric azimuthal motions (Plaut & Busse 2002). We find it convenient to separate the axisymmetric from the non-axisymmetric flow:

$$\boldsymbol{u} = \widetilde{\boldsymbol{u}} + \overline{\boldsymbol{u}} = \widetilde{u}_s(s,\phi,t)\,\hat{\boldsymbol{s}} + [\overline{u}_\phi(s,t) + \widetilde{u}_\phi(s,\phi,t)]\hat{\boldsymbol{\phi}}.$$

denoting the average over ϕ by an overbar. Similarly, the vertical component of the vorticity is written $\zeta(s,\phi,t) = \widetilde{\zeta}(s,\phi,t) + \overline{\zeta}(s,t)$, where $\overline{\zeta} = s^{-1}\partial(s\overline{u}_\phi)/\partial s$ and $\widetilde{\zeta} = s^{-1}[\partial(s\widetilde{u}_\phi)/\partial s - \partial\widetilde{u}_s/\partial\phi]$ are associated respectively with the axisymmetric and the non-axisymmetric flows. On the one hand, we infer an equation for the non-axisymmetric motions – which we call for brevity the 'convective' motions – from the non-axisymmetric part of the vorticity equation (3.8) $-\overline{(3.8)}$

$$\frac{\partial\widetilde{\zeta}}{\partial t} + (\widetilde{\boldsymbol{u}}\cdot\nabla)\zeta + \frac{\overline{u}_\phi}{s}\frac{\partial\widetilde{\zeta}}{\partial\phi} - \overline{(\widetilde{\boldsymbol{u}}\cdot\nabla)\widetilde{\zeta}} + \beta\widetilde{u}_s = \frac{R}{P}\frac{\partial}{\partial\phi}\langle\Theta\rangle_z + \nabla_H^2\widetilde{\zeta} + E^{-1/2}\Phi(\widetilde{\boldsymbol{u}}). \tag{3.10}$$

On the other hand, the zonal wind equation comes from the axisymmetric component of the momentum equation (3.2), projected along $\hat{\boldsymbol{\phi}}$ and integrated along the z-axis. We thus avoid one derivation of the ψ function. As the buoyancy and pressure terms vanish, we obtain (Aubert *et al.* 2001)

$$\frac{\partial\overline{u}_\phi}{\partial t} + \overline{(\widetilde{\boldsymbol{u}}\cdot\nabla)\,\widetilde{u}_\phi} = \frac{\partial}{\partial s}\left[\frac{1}{s}\frac{\partial}{\partial s}\left(s\overline{u}_\phi\right)\right] - \sqrt{\frac{r_o}{H}}\frac{\overline{u}_\phi}{E^{1/2}H}. \tag{3.11}$$

The no-slip boundary condition yields

$$\overline{u}_\phi = 0 \text{ at } s = s_i, r_0. \tag{3.12}$$

In the study by Aubert *et al.* (2003), Ekman pumping is only included in equation (3.11) for the axisymmetric flow (i.e. they considered $\Phi(\widetilde{\boldsymbol{u}}) = 0$). Here we take into account this effect for the whole geostrophic flow. We will present in § 3.4 a comparison of the numerical simulations with and without Ekman pumping at the onset of convection.

3.3. *Quasi-geostrophic approximation of the heat equation*

We now transform the heat equation into a two-dimensional equation using the quasi-geostrophic approximation. Integrating (3.3) along the $\hat{\boldsymbol{z}}$-direction in the bulk of the fluid gives at leading order

$$\left[\frac{\partial}{\partial t} + (\boldsymbol{u}\cdot\nabla) - P^{-1}\nabla_H^2\right]\langle\Theta\rangle_z + \widetilde{u}_s\frac{\mathrm{d}}{\mathrm{d}s}\left\langle T_{\mathrm{cond}}^{\mathrm{ic}}\right\rangle_z = -\left\langle u_z\frac{\partial T}{\partial z}\right\rangle_z + \frac{P^{-1}}{2H}\left[\frac{\partial\Theta}{\partial z}\right]_{-H}^{+H}. \tag{3.13}$$

On the right-hand side of (3.13), we have put together the advection and diffusion terms along $\hat{\boldsymbol{z}}$. Taking into account that the vertical velocity is linear along the $\hat{\boldsymbol{z}}$-axis, we can estimate the advection term as

$$\left\langle u_z\frac{\partial T}{\partial z}\right\rangle_z = -\frac{\eta}{H}\widetilde{u}_s\left[\frac{T_o}{\Delta T} - \langle T\rangle_z\right].$$

Since the typical equatorial size in rapidly rotating convection is small compared to the height $2H$ of a fluid column (Busse 1970, see also § 3.4), the vertical diffusion of temperature is negligible compared to the equatorial diffusion. This is no longer true in the thermal boundary layers on the sphere. A three-dimensional description of Θ

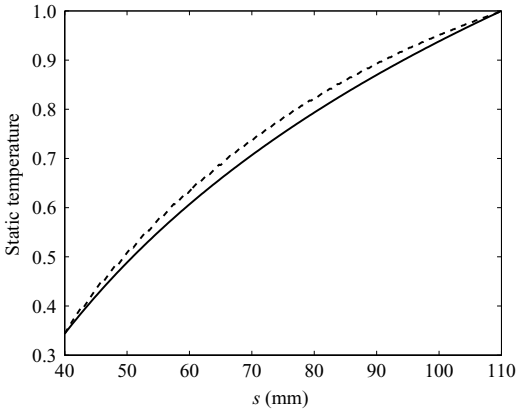

FIGURE 5. $(\langle T^{\rm ic}_{\rm cond}\rangle_z - T_i/\Delta T)$ (dashed line) and $(T^{\rm ic\,2D}_{\rm cond} - T_i/\Delta T)$ (solid lines) as a function of the cylindrical radius s, obtained from equation (3.14). The two profiles are normalized to ΔT.

would thus be necessary to estimate the diffusion of temperature along $\hat{\boldsymbol{z}}$ and the heat flux, at the outer sphere surface, as a function of latitude. The case $P \ll 1$ may be particularly amenable to such a treatment, since the temperature field is diffused away more rapidly than the velocity field (and thus is smoother). A three-dimensional mesh, looser than the equatorial mesh used for the velocity field, could then be used to describe the temperature field, without the computations being too time-demanding.

We have nevertheless chosen to keep a two-dimensional description of Θ that overestimates the equatorial heat flux for a given forcing (vertical heat flux ignored). Then the static temperature profile $\langle T^{\rm ic}_{\rm cond}\rangle_z$ in equation (3.13) does not satisfy the equation $\nabla_H^2 T = 0$. We have approximated this profile by $T^{\rm ic\,2D}_{\rm cond}$, the solution of the latter equation that satisfies the boundary conditions $T^{\rm ic\,2D}_{\rm cond}(s_i) = \langle T^{\rm ic}_{\rm cond}\rangle_z(s_i)$ and $T^{\rm ic\,2D}_{\rm cond}(r_o) = T_o/\Delta T$. This profile is (Aubert *et al.* 2003)

$$T^{\rm ic\,2D}_{\rm cond}(s) = \left\langle T^{\rm ic}_{\rm cond}\right\rangle_z(s_i) + \xi^{\rm ic}\frac{\ln(s/s_i)}{\ln(r_o/s_i)}, \tag{3.14}$$

with $\xi^{\rm ic} = T_o/\Delta T - \langle T^{\rm ic}_{\rm cond}\rangle_z(s_i)$ the 'effective' temperature drop. $T^{\rm ic}_{\rm cond}$ has been calculated numerically with a relaxation method, using the thermal boundary conditions described in § 3.1 (inner cylinder, outer sphere). The calculation gives $\xi^{\rm ic} \simeq 0.656$. We compare in figure 5 the z-integrated three-dimensional profile $\langle T^{\rm ic}_{\rm cond}\rangle_z$ with the two-dimensional static profile $T^{\rm ic\,2D}_{\rm cond}$. One can note that those two profiles are rather similar. That leads us to write the heat equation (3.13) as follows:

$$\frac{\partial}{\partial t}\langle\Theta\rangle_z + (\boldsymbol{u}\cdot\nabla_H)\langle\Theta\rangle_z + \widetilde{u}_s\frac{\mathrm{d}}{\mathrm{d}s}T^{\rm ic\,2D}_{\rm cond} = P^{-1}\nabla_H^2\langle\Theta\rangle_z. \tag{3.15}$$

The temperature perturbation satisfies the boundary conditions

$$\langle\Theta\rangle_z = 0 \text{ at } s = s_i, r_0. \tag{3.16}$$

We use a finite differences (resp. spectral) decomposition in the radial (resp. azimuthal) direction to describe the ψ and $\langle\Theta\rangle_z$ fields. The system ((3.10), (3.11), (3.15)), together with the boundary conditions ((3.5), (3.12), (3.16)), is numerically solved using an implicit Crank–Nicholson scheme for the linear terms, except for the buoyancy term in equation (3.10) and the advection of the static profile $T^{\rm ic\,2D}_{\rm cond}$ in equation (3.15). These two terms, as well as the nonlinear terms, are computed

with an explicit Adams–Bashforth scheme. We have used up to 400 grid points in the radial direction and up to 200 modes in the azimuthal direction.

3.4. *Onset of convection; impact of the Ekman pumping*

We now describe the main characteristics of the instability threshold: we compare linear numerical calculations performed using our quasi-geostrophic model with three-dimensional calculations of the onset of rapidly rotating convection between two spheres.

The onset of thermal convection in rapidly rotating systems with spherical symmetry was first studied by Roberts (1968) and Busse (1970) (internally heated spheres). These approaches describe the most unstable mode as a thermally driven Rossby wave. This result can be extended to thermal convection in a spherical shell in which a temperature difference is maintained between the inner and outer spheres (see e.g. Dormy *et al.* 2004). Then, the wave is localized adjacent to the cylinder tangent to the inner sphere. The parameter $\beta_i = \beta(s_i)$ is evaluated from the height $H_i = H(s_i)$ and the slope $\eta_i = \eta(s_i)$ of the outer boundary at its intersection with the tangent cylinder. Roberts (1968) and Busse (1970) have given the dependence of the critical parameters (the Rayleigh number R_c, the wavenumber m_c and the frequency ω_c) as functions of the dimensionless parameters:

$$R_c \sim (P\omega_c)^2 \sim m_c^4 \sim \left[\frac{\beta_i}{1+P^{-1}}\right]^{4/3} = \left[\frac{\eta_i}{E\,H_i(1+P^{-1})}\right]^{4/3}. \tag{3.17}$$

For large values of P, one has $1 + P^{-1} \simeq 1$ so that the diffusivity governing the critical parameters in (3.17) is the kinematic viscosity. As the Prandtl number decreases, the convective cells become more and more spiral (Zhang 1992*b*; Yano 1992). For even weaker values of P, Zhang & Busse (1987) have shown that the thermal instability can take the form of an equatorially trapped inertial wave (see further studies by Zhang 1992*a*, 1993). Numerical studies by Ardes, Busse & Wicht (1997), and more recently by Plaut & Busse (2005), have shown that this kind of wave requires a relatively moderate rotation rate to appear ($2 \times 10^{-2} P^2 < E \ll 1$).

In our experimental study with gallium ($P = 0.025$) the rotation rates and temperature contrasts correspond to convection that develops first as spiral modes. One has $1 + P^{-1} \simeq P^{-1}$ so that the role played by the Ekman number in equation (3.17) for large P is taken over by the thermal Ekman number, and the convection onset depends now on the thermal diffusivity. This leads to much larger typical values of ΔT_c in gallium than in water (see table 1).

Gillet & Jones (2006) give an extensive justification of the quasi-geostrophic approximation at the onset of convection. We complete their work by noting that incorporating the Ekman pumping term in the model improves the agreement with a fully three-dimensional modelling. Dormy *et al.* (2004) studied the onset of convection between two isothermal spheres (radii r_i and r_o, temperatures T_i and T_o) in the differential heating case for $P = 1$; their static temperature profile is

$$T^{\mathrm{is}}_{\mathrm{cond}}(r) = \frac{r_o T_o - r_i T_i}{d\,\Delta T} - \frac{r_o r_i}{r d},$$

where the superscript 'is' stands for an inner sphere. Note that in the quasi-geostrophic representation the internal boundary is cylindrical, as opposed to spherical in the three-dimensional computations. In order to make the comparison relevant, we have

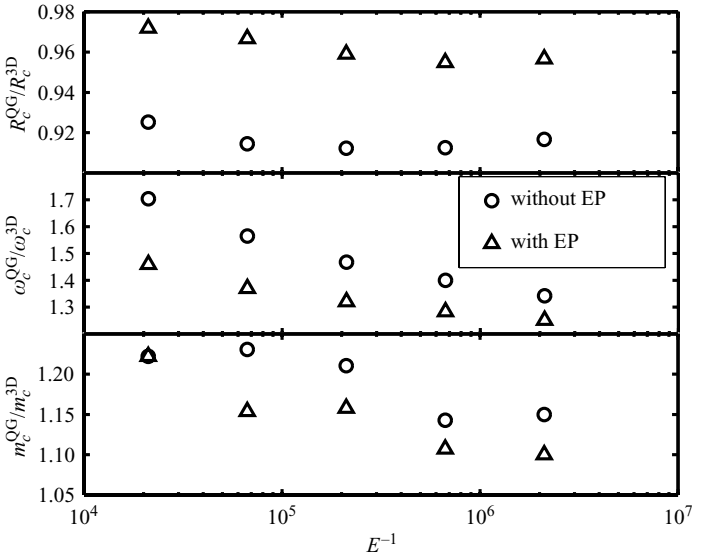

FIGURE 6. Numerical simulations at the onset of convection in a rapidly rotating shell, in the differential heating case, with no-slip boundary conditions, for $P = 1$ and $s_i/r_o = 0.35$. Ratios between the critical parameters (R_c, ω_c, m_c) obtained with the quasi-geostrophic simulations, and the critical parameters obtained with the three-dimensional simulations by Dormy *et al.* (2004) using no-slip boundary conditions, as a function of E^{-1}. Calculations are performed with (triangles) and without (circles) the Ekman pumping (EP) in the quasi-geostrophic approximation case, with $\xi^{is} = 0.453$.

imposed in our simulation the following thermal boundary conditions

$$T_{\text{cond}}^{\text{is 2D}}(r_o) = \frac{T_o}{\Delta T} \text{ and } T_{\text{cond}}^{\text{is 2D}}(s_i) = \left\langle T_{\text{cond}}^{\text{is}} \right\rangle_z (s_i),$$

which gives (Aubert *et al.* 2003):

with

$$\left.\begin{aligned} T_{\text{cond}}^{\text{is 2D}}(s) &= \left\langle T_{\text{cond}}^{\text{is}} \right\rangle_z (s_i) + \xi^{\text{is}} \frac{\ln(s/s_i)}{\ln(r_o/s_i)}, \\ \xi^{\text{is}} &= \frac{s_i}{d}\left[\frac{r_o}{H_i}\,\text{arcsh}\left(\frac{H_i}{s_i}\right) - 1\right]. \end{aligned}\right\} \tag{3.18}$$

For the aspect ratio $s_i/r_o = 0.35$, we find in the case of both inner and outer spherical boundaries $\xi^{is} \simeq 0.453$ (instead of $\xi^{ic} \simeq 0.656$ in the previous experimental case with an inner cylinder and an outer sphere, cf. § 3.3). Using also the study by Dormy *et al.* (2004) down to $E = 4.74 \times 10^{-7}$, Aubert *et al.* (2003) had found that the quasi-geostrophic approach provides a good estimate of the parameters at onset of convection (in their study the Ekman pumping was only introduced for the axisymmetric motions and this played no role for the onset of convection). Down to similar values of the Ekman number we complete this comparison by including the Ekman pumping term for the non-axisymmetric modes, as shown in figure 6. It appears that the quasi-geostrophic calculation for R_c converges toward a value closer to the correct one when the Ekman pumping is included. The wavenumbers are similarly less overestimated when the Ekman pumping is included (10 % versus 15 % discrepancies at the lowest values of E) and consequently the error made in the frequency is also reduced.

	$P=7$			$P=0.025$		
	R_c	m_c	ω_c	R_c	m_c	ω_c
Without Ekman pumping	1.39×10^7	24	328	6.09×10^6	13	13000
With Ekman pumping	1.31×10^7	22	276	6.71×10^6	14	12680

TABLE 4. Critical parameters at the onset of convection obtained from quasi-geostrophic numerical simulations, with and without Ekman pumping, for $P=7$ ($E=6.5\times10^{-6}$), $P=0.025$ ($E=1.95\times10^{-6}$), and with $s_i/r_o=4/11$ ($\xi^{ic}=0.656$).

P	E ($\times10^{-6}$)	Ω (r.p.m.)	R_c ($\times10^6$)	ΔT_c (K)	ω_c	τ_c (s)	m_c
	2.92	200	4.29	11.6	9760	10.7	12
0.025	1.95	300	6.76	8.2	12720	8.2	14
	0.97	600	15.19	4.6	20080	5.2	17
	9.74	200	8	0.54	210	146.6	20
	6.50	300	13.2	0.40	276	111.5	22
7	4.87	400	19	0.32	336	91.6	24
	3.25	600	31.7	0.24	441	69.8	27
	2.44	800	38.6	0.19	536	57.4	30

TABLE 5. Critical values at the onset of convection (Rayleigh number, temperature difference, frequency, period $\tau_c=2\pi d^2(\nu\omega_c)^{-1}$ and wavenumber of the thermal Rossby wave) as a function of the rotation rate Ω (or E) used in the experiments, for gallium ($P=0.025$) and for water ($P=7$). Values obtained from quasi-geostrophic numerical simulations with the Ekman pumping term included.

The influence of the no-slip boundary condition on the convection threshold depends on P. We notice in table 4 a destabilizing effect at $P=7$, as opposed to a stabilizing effect at $P=0.025$. This agrees qualitatively with both the three-dimensional computations and the analytical study of Zhang & Jones (1992). In accordance with their study, we also find a more pronounced decrease in the frequency at large values of P, and opposite effects on the wavenumber: an increase (decrease) at weak (large) Prandtl numbers. However Zhang & Jones (1992) show an Ekman friction impact on the critical parameters of $O(E^{*1/6})$, which we do not retrieve in figure 6.

The critical parameters at the convection threshold for the range of parameters of our experiment are determined numerically with our simulations; they are given in table 5. The values of the critical Rayleigh numbers R_c determined numerically will be used as an input for the experiments, as the onset of convection cannot be accurately determined in our experimental set-up.

4. Thermal convection in a rapidly rotating spherical shell in a low-Prandtl-number fluid

4.1. *Velocity measurements in convection experiments performed in gallium*

Our experiment in liquid gallium remains in a range of forcings close to critical ($R/R_c\leqslant6$), because of the high thermal diffusivity of liquid metals such as gallium. Thus the mean temperature profiles should remain close to the conductive one. The flow is turbulent however, and we measure large velocities, up to $3\,\mathrm{cm\,s^{-1}}$. In their liquid sodium experiments, Shew & Lathrop (2005) were able to estimate the heat flux, and found that the Nusselt number, ratio of the total heat flux to the heat flux

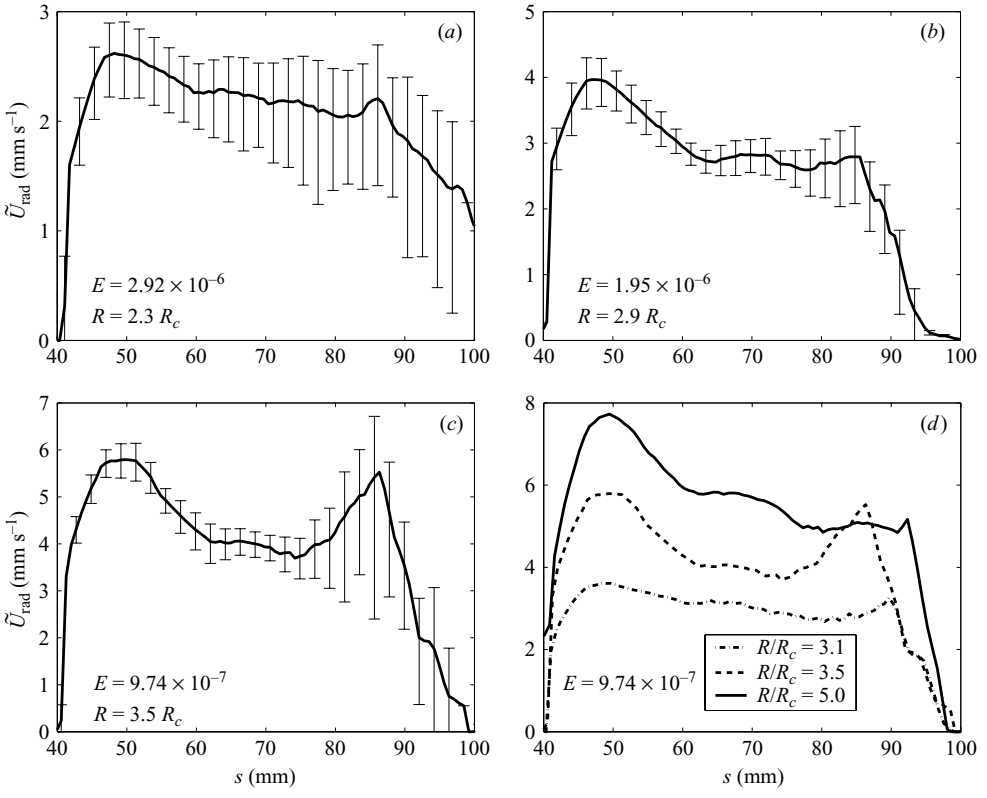

FIGURE 7. R.m.s. radial velocity profiles $\widetilde{U}_{\rm rad}$ as a function of radius s measured during convection experiments performed in gallium for various E and various R/R_c. The measurements are averaged over a period τ from 200 to 400 s in (a)–(d).

carried along the conductive temperature profile, is of order 2 at maximum. They have nevertheless indirectly detected velocities up to about ten times larger than ours. This supports the statement that for $P \ll 1$, the convection close to onset produces highly turbulent flows.

The velocity profiles $\widetilde{U}_{\rm rad}(s)$ for the r.m.s. radial motions and $\overline{U}_{\rm zon}(s)$ for the azimuthal flow, obtained from measurements in gallium after averaging over long time intervals, are illustrated in figures 7 and 8. These averages change very little throughout all experimental runs with gallium. We compare velocities that are measured at different Ekman and Rayleigh numbers.

At first order, the shapes of the r.m.s. radial velocity profiles on the one hand (figure 7) and the shapes of the azimuthal profiles on the other hand (figure 8), remain identical in the range of parameters that we cover, the amplitude of the velocities depending on the forcing (R/R_c). The maximum of the r.m.s. radial velocity, relatively close to the inner cylinder, is followed by a smooth decrease towards the outer boundary. The mean azimuthal flow, the so-called zonal flow, is retrograde near the inner cylinder and then increases in a broad region to eventually change into a small prograde zonal flow at the outer boundary.

At second order, it can also be seen in figures 7(d) and 8(d), where E is fixed and R/R_c increased, that the radius at which the r.m.s. velocity is maximum (or similarly at which the zonal flow is minimum) increases as a function of the forcing. In other

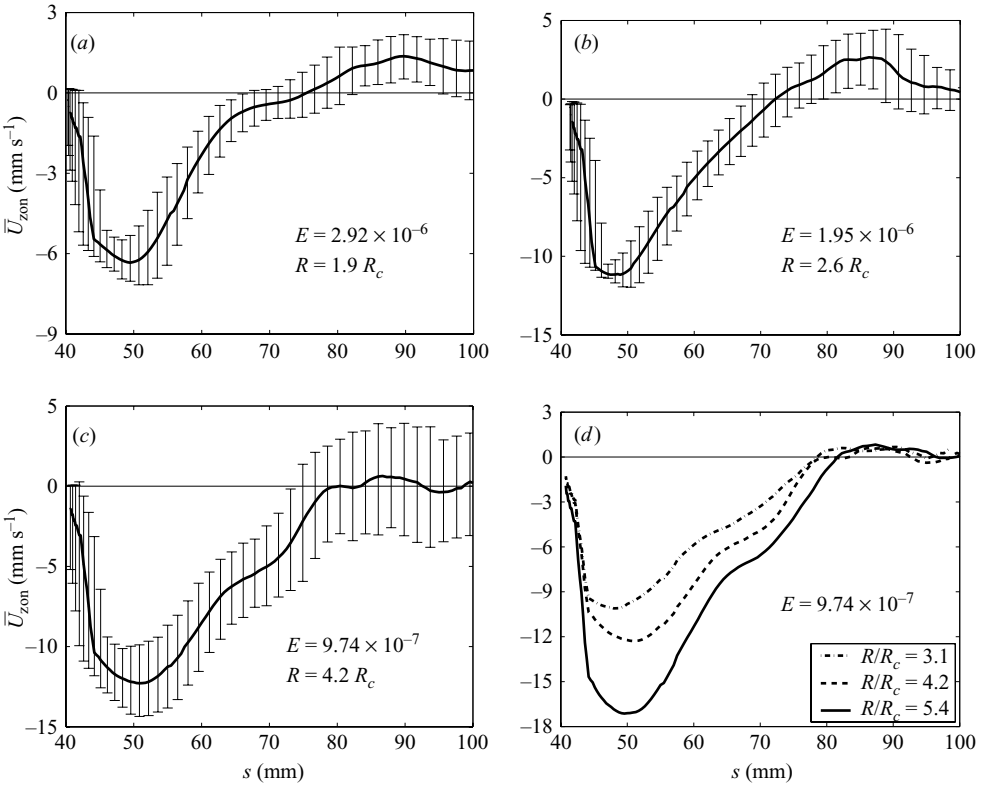

FIGURE 8. Zonal velocity profiles $\overline{U}_{zon}$ as a function of radius s measured during convection experiments performed in gallium with various E and various R/R_c. The measurements are averaged over a period τ from 200 to 400 s in (a)–(d).

words, the size of the convective zone increases with R/R_c. It is not easy to disentangle the possible influence of the Ekman number (or more plausibly the thermal Ekman number) on the size of the convective region or the width of the retrograde zonal jet – figures 7(a,b,c) and 8(a,b,c) – from the effect of the forcing strength. These observations are discussed in § 4.3. Note that the amplitude of the zonal flow is about three times the amplitude of the radial flow in these gallium experiments.

4.2. *A comparison based on convective motions*

Following Aubert *et al.* (2003), we compare velocities measured in the experiments with velocities obtained in the quasi-geostrophic numerical models for a given value of the convection vigour, which we estimate here as

$$\widetilde{U} = \left[\frac{1}{V} \int_V \widetilde{U}_{\mathrm{rad}}(s)^2 \, \mathrm{d}V \right]^{1/2},$$

where V is the total volume filled with fluid and $\widetilde{U}_{\mathrm{rad}}(s)$ is defined in § 2.2. Note that $\widetilde{U}$ is also a global kinematic Reynolds number based on the thickness d of the shell. Similarly we measure the zonal wind intensity as

$$\overline{U} = \left[\frac{1}{V} \int_V \overline{U}_{\mathrm{zon}}(s)^2 \, \mathrm{d}V \right]^{1/2}.$$

Such definitions suit water measurements where the profiles are available for all radii (see § 5). However, integrating over the whole radius is not possible in gallium since the ultrasonic apparatus fails to measure velocities close to the outer sphere, as seen for example in figure 3(a,b). For comparisons between computations and experiments in gallium we use instead $\widetilde{U}^* = \max\{\widetilde{U}_{\rm rad}(s)\}$ and $\overline{U}^* = \max\{-\overline{U}_{\rm zon}(s)\}$. Such definitions of the characteristic radial and zonal velocities were chosen because they turn out to be the most reproducible experimental data. The velocity profiles in gallium, $\widetilde{U}_{\rm rad}$ and $\overline{U}_{\rm zon}$, are smooth, stable in time, and gently evolve in the explored range of parameters. Then the influence of the norm is not crucial, as we verify with our quasi-geostrophic numerical calculation (see figure 12).

A comparison between the velocities measured in a gallium experiment and computed in the corresponding quasi-geostrophic simulation is shown in figure 9. In figure 9(a,b), we compare, for a given value of $\widetilde{U}^*$, the spatio-temporal evolution of the radial velocity $\widetilde{u}_s(s,t)$ measured experimentally to the quasi-geostrophic numerical reconstruction of the same velocity component. From these, we extract the experimental and numerical r.m.s. radial velocity profiles $\widetilde{U}_{\rm rad}(s)$, shown in figure 9($c$). For the same value of $\widetilde{U}^*$, figure 9(d) shows a comparison between the experimental and numerical zonal profiles $\overline{U}_{\rm zon}(s)$. Since we were not able to measure both profiles simultaneously with our ultrasonic Doppler velocimetry technique, zonal and radial experimental profiles come from different experimental runs but with the same imposed temperature difference ΔT. At first order, figure 9(a,b,c) displays a remarkable agreement between experiments and numerics: for a given experimental $\widetilde{U}^*$, the quasi-geostrophic simulation reproduces the correct shape of the experimental radial profile as well as the experimental amplitude and shape of the zonal wind. On the other hand, we find that for a given value of R/R_c, convection is more vigorous in the quasi-geostrophic calculation than in the experiment. As mentioned in § 3.3, thermal boundary layers attached to the outer sphere are not modelled in our simulations. As a result, experiments and numerical simulations conducted at the same Rayleigh number do not match.

As mentioned in § 4.1, the convective activity is concentrated in the first few centimetres near the inner cylinder (figure 9a,b) and is associated with a strong retrograde zonal flow (figure 9c). Notice however that for a given $\widetilde{U}^*$, the convection seems to occupy a larger area in the experiment than in the quasi-geostrophic simulation. The velocity measurements also show a – poorly constrained – prograde zonal flow arising near the outer sphere, in qualitative agreement with the quasi-geostrophic numerical calculations.

A retrograde zonal flow near the inner cylinder has also been predicted from an analytical study of weak-amplitude convection (Plaut & Busse 2005). Herrmann & Busse (1997) and Plaut & Busse (2002) described the associated vacillating convection arising in the weakly nonlinear regime at low P. Figure 10 illustrates this behaviour for $E = 1.95 \times 10^{-6}$, in numerically calculated time sequences of the kinetic energies

$$\widetilde{\mathscr{E}}(t) = \frac{1}{V}\int_V \widetilde{\boldsymbol{u}}(s,\phi,t)^2 \,\mathrm{d}V \quad \text{and} \quad \overline{\mathscr{E}}(t) = \frac{1}{V}\int_V \overline{\boldsymbol{u}}(s,t)^2 \,\mathrm{d}V,$$

associated respectively with the r.m.s. and the mean zonal flows. At $R/R_c = 1.4$, any periodicity in the time evolution is lost.

We now interpret the retrograde zonal flow near the inner cylinder in the fully developed convection regime. The observed shear flows are associated with a ring of anticyclones around the inner cylinder and a – less pronounced – cyclonic area at

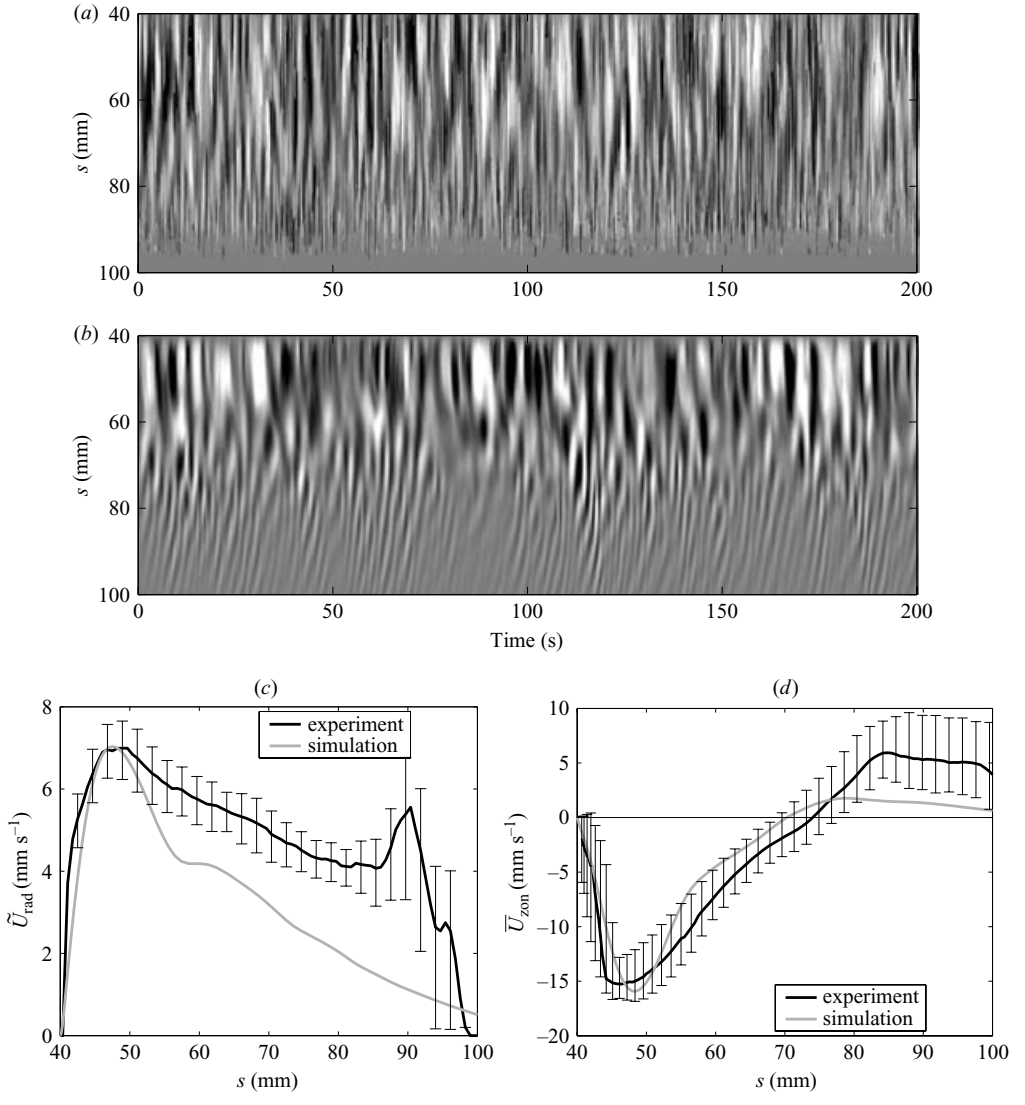

FIGURE 9. (a, b) Radial velocity as a function of time and radius for $P = 0.025$, $E = 9.74 \times 10^{-7}$ and a given value $\widetilde{U}^* = 1630$ (equivalent to 7 mm s^{-1}). From ultrasonic Doppler velocimetry (a) and quasi-geostrophic simulations (b). The colour scale goes from -10 (black) to $+10$ mm s^{-1} (white). Rayleigh numbers are respectively $R = 4.7\ R_c$ (experiment) and $R = 2\ R_c$ (simulation). (c) Corresponding radial velocity profiles $\widetilde{U}_{\rm rad}(s)$, and ($d$) corresponding zonal velocity profiles $\overline{U}_{\rm zon}(s)$, from an experiment (black) and a quasi-geostrophic simulation (grey).

larger radii. This relationship between the signs of the vorticity field and of the zonal flow can be accounted for by the conservation of the potential vorticity $\zeta - 2\,\Omega \ln H$, a quantity kept constant when the sources and sinks of vorticity, on the right-hand side of (3.8), can be neglected (Aubert *et al.* 2001, 2002). As convection becomes more intense a dissymmetry builds up between thin and fast upwellings on the one hand, and wider and slower downwellings on the other hand (the former driving the dynamics in terms of vorticity). The upwellings gain negative relative vorticity (they

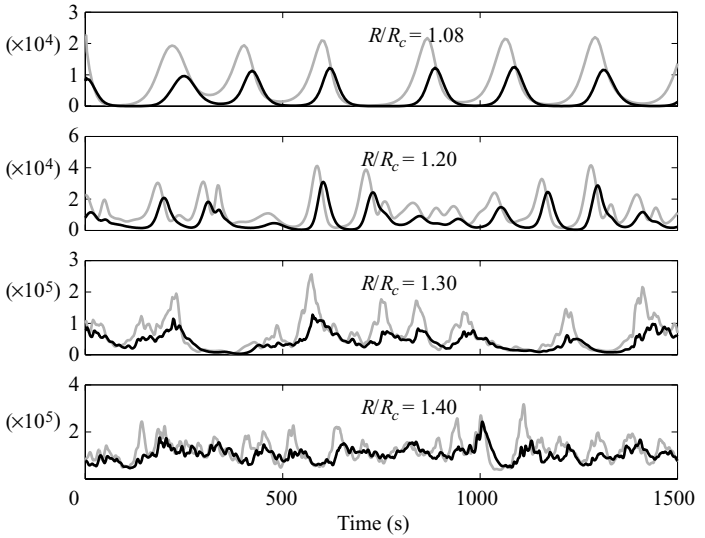

FIGURE 10. Time series of the non-axisymmetric motions $\widetilde{\mathscr{E}}(t)$ (grey) and the axisymmetric motions $\overline{\mathscr{E}}(t)$ (black), as convection departs from onset (increasing R/R_c values), from quasi-geostrophic calculations at $P = 0.025$, $E = 1.95 \times 10^{-6}$.

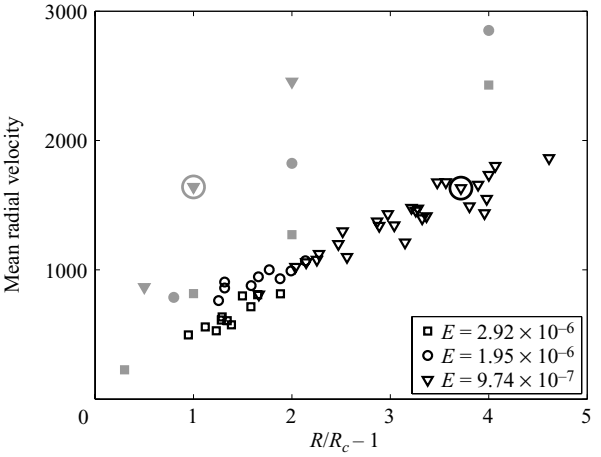

FIGURE 11. Amplitude of the mean radial velocity $\widetilde{U}^*$ (Reynolds number) as a function of $(R/R_c - 1)$, for $P = 0.025$ and different values of E. From experimental ultrasonic Doppler velocimetry (open symbols) and numerical simulations (grey symbols). The grey symbols are at the same E value as the corresponding black symbols. The dispersion between experimental points gives a hint of the error bars. The circled symbols refer to the profiles of figure 9(*b*).

are anticyclonic) because the height of a fluid column is reduced as it moves away from the inner cylinder.

All the experimental measurements and numerical estimations of the radial motions $\widetilde{U}^*$ are compiled in figure 11. Again, the numerical simulations overestimate $\widetilde{U}^*$ because of the lack of thermal boundary layers as mentioned previously. All the experiments, remarkably, align on the same line as a function of $(R/R_c - 1)$; although the parameter $(R/R_c - 1)$ seems sufficient to scale the vigour of the convection

whatever the Ekman number, the quasi-geostrophic simulation suggests that this is true only at first order. The shrinking experimental range of R/R_c values as E becomes larger is partly responsible for that picture, which must be considered with caution. This point will be detailed in § 4.3.

4.3. *Latitudinal length scale and amplitude of the mean zonal flow*

In our gallium experiments, the energy of the mean zonal flow makes up most of the kinetic energy, as in models of turbulence in a β-plane. We extract from the equation (3.8) the Rhines balance between the Coriolis and the nonlinear inertial terms:

$$\widetilde{u}_s \frac{\partial \overline{\zeta}}{\partial s} \sim \beta \widetilde{u}_s. \tag{4.1}$$

Introducing the Rhines scale ℓ_β associated with the radial shear of the mean zonal flow, we evaluate the mean vorticity as $\overline{\zeta} \sim \overline{U}/\ell_\beta$, and approximate (4.1) by

$$\widetilde{U} \frac{\overline{U}}{\ell_\beta^2} \sim \beta \widetilde{U}. \tag{4.2}$$

The Rhines scale can then be written as

$$\ell_\beta \sim \sqrt{\frac{\overline{U}}{\beta(s)}}. \tag{4.3}$$

We can combine this result with equation (3.11) where we neglect the first term on the right-hand side (volume friction). This term, indeed, plays almost no part in convection onset, where the scaling is derived from the thermal diffusivity, and it should be even more negligible in fully developed convection, where the typical length scale increases. Thus the main brake on the zonal wind generation consists of the Ekman friction at the top and bottom boundaries, whilst the main source of zonal wind in equation (3.11) is the axisymmetric component of the Reynolds stress $\overline{(\widetilde{\boldsymbol{u}} \cdot \boldsymbol{\nabla})\widetilde{u}_\phi} \sim \widetilde{U}^2/\ell_\beta$. Then the balance between Reynolds stress and Ekman friction in equation (3.11) is expressed using (3.9) as

$$\frac{\widetilde{U}^2}{\ell_\beta} \sim \sqrt{\frac{r_o \beta}{2sH}}\, \overline{U}. \tag{4.4}$$

The increase of $\beta(s)$ with s is a distinctive feature of the full sphere geometry: here its impact on the Reynolds term through ℓ_β (in $\beta(s)^{1/2}$ on the left-hand side of (4.4)), is exactly compensated by its impact on the top and bottom friction term (in $\beta(s)^{1/2}$ on the right-hand side of (4.4)). Together with the expression (4.3) for the Rhines scale, equation (4.4) leads to

$$\widetilde{U}^2 \sim \sqrt{\frac{r_o}{2sH}}\, \overline{U}^{3/2}. \tag{4.5}$$

Finally $\beta(s)$ disappears in (4.5), so that this scaling law holds irrespective of the rotation rate. Note that the viscosity still plays a role (the dimensionless velocities are scaled using the viscous time scale d^2/ν), since the Ekman friction on the zonal flow is a key point when deriving this scaling law. Equation (4.5) can be rewritten

$$\left(\frac{r_o}{2sH}\right)^{1/3} \overline{U} \sim \widetilde{U}^{4/3}. \tag{4.6}$$

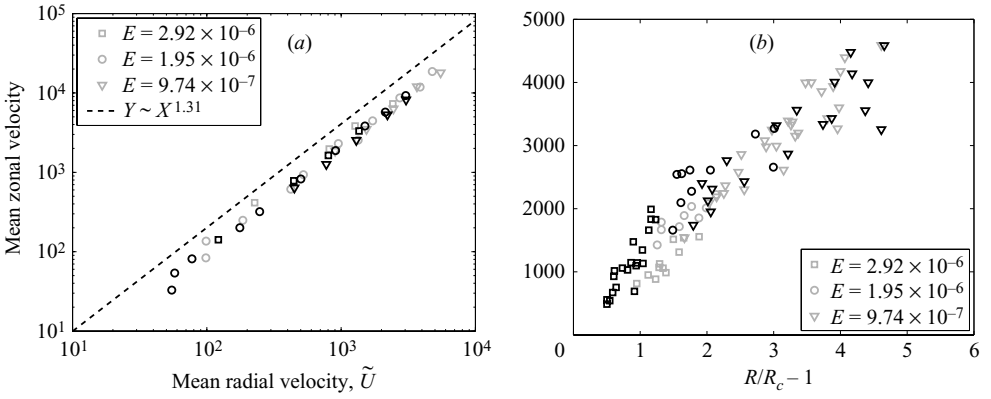

FIGURE 12. (*a*) Mean zonal velocity as a function of the mean radial velocity obtained from numerical simulations, for $P = 0.025$ and different values of E. Both norms presented in §4.2 have been used: $\{\widetilde{U}, \overline{U}\}$ from integrated profiles in volume (black), and $\{\widetilde{U}^*, \overline{U}^*\}$ from their extremum value (grey). The best fit, $\overline{U} = (0.25 \pm 0.02)\ \widetilde{U}^{1.31 \pm 0.06}$ is computed from all the simulations, except the three closer to the onset at $E = 1.95 \times 10^{-6}$ which present vacillating convection (see figure 10). (*b*) Mean zonal velocity $\overline{U}^*$ (black symbols) and derived law $0.25\ \widetilde{U}^{*1.31}$ (grey symbols) obtained in (*a*) as a function of $R/R_c - 1$, from experimental measurements performed in gallium for several E.

Interestingly the geometrical prefactor in front of $\overline{U}$ in equation (4.6) varies very weakly as a function of s (if we except the area close to the equator where it diverges). The variation is only 12% in a length in s covering 91% of the whole gap d. It is then reasonable to neglect the radial evolution of the prefactor in (4.6), so that we infer the relation

$$\overline{U} \sim \widetilde{U}^{4/3}. \tag{4.7}$$

Figure 12(*a*) shows that the relation (4.7) is numerically satisfied with the evolution of the zonal wind as a function of the radial velocity with an exponent 1.31, close to the exponent 4/3. One can also check that this trend does not depend on the choice of the velocity norms – either $\{\widetilde{U}, \overline{U}\}$ or $\{\widetilde{U}^*, \overline{U}^*\}$. Similarly, figure 12(*b*) demonstrates that the zonal and radial velocities measured in the gallium experiments also closely follow the prediction (4.7).

Coming back to the definition of ℓ_β obtained in (4.3), it appears that the length scale associated with the radial shear of the zonal flow should increase as $\overline{U}^{1/2}$. The vorticity maps and the associated mean zonal flows in figure 13(*a–d*) obtained in the numerical simulations do indeed indicate that this length scale increases with the vigour of the convection. That increase is further demonstrated in figure 13(*e*, *f*) where it is seen that the size of the convective zone deduced both from the radial and the azimuthal profiles increases as a function of R/R_c. Looking quantitatively at the results of these simulations, ℓ_β does not increase as rapidly as $\overline{U}^{1/2}$ however. We attribute this observation, which conflicts with the confirmation of (4.7), to the increase of β with s as the main zonal jet is enlarged. In other words the reverse cascade occurs, but the Rhines scale toward which it converges is decreased by the curvature of the spherical boundary. The growth of ℓ_β is also limited because it is already relatively large in comparison with the gap d. This kind of experiment would require a faster rotation rate – or a larger size – in order to decrease the Rhines scale.

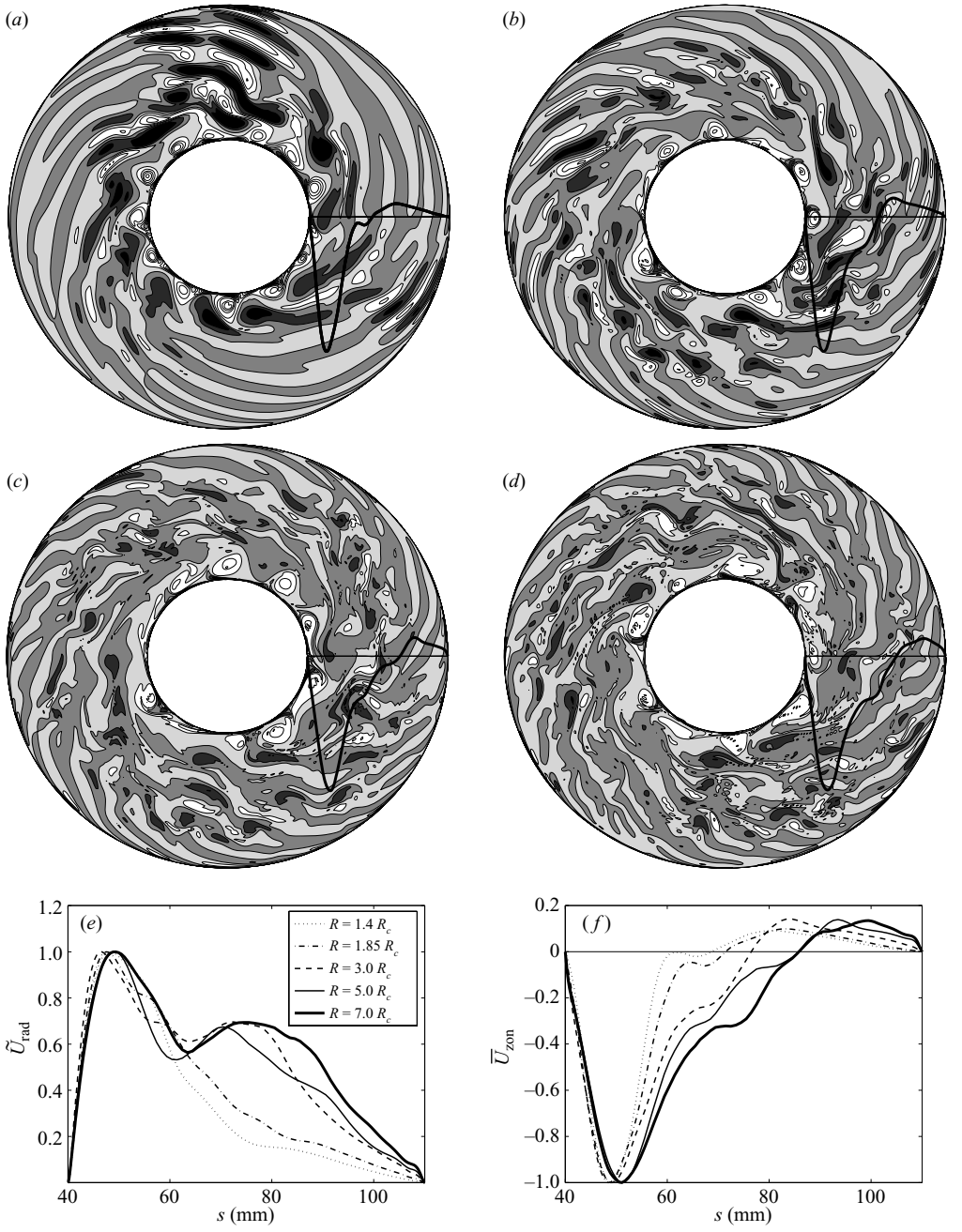

FIGURE 13. (*a–d*) Normalized vorticity maps in the equatorial plane of the rotating sphere obtained from numerical simulation for $P = 0.025$, $E = 1.95 \times 10^{-6}$, and respectively $R/R_c = 1.85$, 3, 5 and 7. The colour scale is clipped from -0.2 (white) to $+0.2$ (black) in order to focus on the convection outside the boundary layers – where the vorticity field is saturated. Superimposed on the vortices, the mean zonal flow is drawn with a black solid line as a function of radius. (*e*, *f*) Normalized profiles of the radial velocity $\widetilde{U}_{\rm rad}$ and the zonal velocity $\overline{U}_{\rm zon}$ as a function of radius s, corresponding to the numerical simulations shown in (*a–d*) plus one at $R/R_c = 1.4$. The extremum velocities for the calculations performed at $R/R_c = 1.4$, 1.85, 3, 5 and 7 are respectively $\widetilde{U}^* =$ 582, 857, 1427, 2711, 3327 and $\overline{U}^* =$ 893, 2138, 4589, 9415, 12667.

With smaller columns, one would not only reduce the effect of curvature, but also increase the range of admissible length scales.

Note finally that looking at radial profiles only we miss part of the information about the typical length scale. In particular we detect in figure 13(*a–d*) an elongation of the vortices along $\hat{\phi}$ at the larger forcings. We understand this as a signature of the β-plane anisotropy associated with the zonal wind generation (e.g. Read *et al.* 2004). As a consequence the vorticity field becomes increasingly dominated by the radial shear of the azimuthal flow. We have tried to distinguish between the radial and azimuthal components of the non-zonal motions numerically, but it amounts only to a very tiny effect. At larger forcing however a more detailed scaling might be needed, where one distinguishes between the radial and azimuthal r.m.s. motions and length scales.

5. Thermal convection in a rapidly rotating spherical shell in a high-Prandtl-number fluid

5.1. *Velocity measurements in convection experiments performed in water*

We now compare the experiments performed in water ($P = 7$) with our numerical simulations. As ΔT_c is much smaller in water than gallium (see table 5), highly supercritical convection is studied. Our measurements in gallium and in water allow us to document differences between rotating convection at respectively low and large Prandtl number.

In convection in water at moderate R/R_c, a much smaller part of the kinetic energy is transferred to the mean zonal flow. We thus expect a scenario different from the one that leads to the inertial regime, characterized by the Rhines scale ℓ_β (see § 4.3). As long as $\overline{\mathscr{E}} \leqslant \widetilde{\mathscr{E}}$, Danilov & Gurarie (2004) suggest that the enlargement of the cells is stopped by the external friction for each vortex, which means that the reverse cascade does not occur. Exploring this parameter regime, Gillet & Jones (2006) find that the jet length remains close to the critical size ℓ_c (see § 5.2). Increasing R/R_c further, if $\overline{\mathscr{E}}$ grows faster than $\widetilde{\mathscr{E}}$, the forcing will necessarily reach a level at which the kinetic energy transferred into the zonal wind will dominate its convective cell source. Then we expect the Rhines scenario to come back (see § 5.3).

Convective velocities are smaller in water than in gallium since they are scaled by the kinematic viscosity, which is much lower than the corresponding scaling parameter in gallium, which is its thermal diffusivity κ. The viscous term plays a role at the onset and it keeps this role as long as the typical length scale of the convective motions has not significantly increased. Figure 14 shows typical measurements of velocities performed in water in this regime where $R \leqslant 40R_c$. We find that for moderate Rayleigh number $R \leqslant 40R_c$, the energy of the zonal motions makes up a small fraction of the total energy as can be seen directly by comparing the velocities in figures 14(*b*) and 14(*c*). As in the experiments in gallium, most of the radial kinetic energy is confined to the convective zone close to the inner cylinder (figure 14*a*). Extracting mean zonal velocities from spatio-temporal transverse velocity measurements, in these experiments in water where $R \leqslant 40R_c$, is rather challenging since $\widetilde{U} \gg \overline{U}$. Figure 14(*c–e*) demonstrates however that averaging the velocity profiles long enough in time enables us to reconstruct mean zonal flows. The zonal velocities are highly time-dependent and composed of multiple zonal jets, alternatively prograde and retrograde as a function of the radius. The various tests of signal processing that we have performed also indicate that the characteristic duration of these zonal jets is of

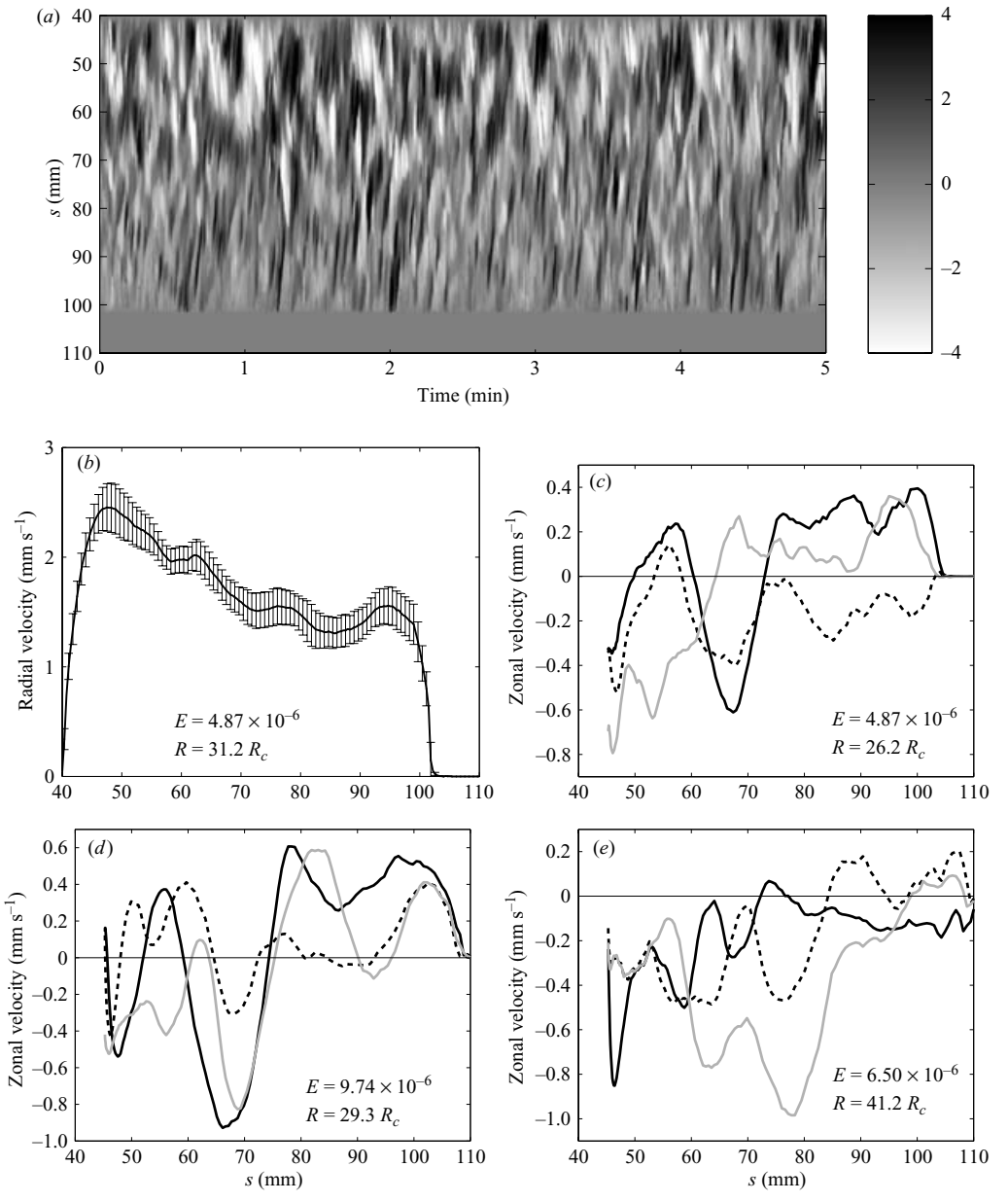

FIGURE 14. Radial and zonal velocity profiles obtained during convection experiments performed in water ($P = 7$) at various E and R/R_c. (*a*) Measured velocity $u_s(s,t)$ in mm s^{-1} as a function of time and radius with $E = 4.87 \times 10^{-6}$, $R = 31.2\ R_c$. (*b*) Radial profile $\widetilde{U}_{\rm rad}(s)$ extracted from the time series in (*a*). (*c–e*) Zonal profiles $\overline{U}_{\rm zon}(s)$ for various E and R/R_c. The measurements are extracted from time series 200 s long. The black, dashed and grey lines are independent averages in time of the mean zonal flow, obtained after processing a 50 s long record.

order 50 s, e.g. 5 to 10 times the characteristic vortex turnover time. These jets occur on the convective vortex length scale ℓ_c, and this regime lasts to $R \leqslant 40 R_c$.

Figures 15 and 16 show examples of velocity profiles as the Rayleigh number becomes larger than about 40 times critical. As we can observe in particular in

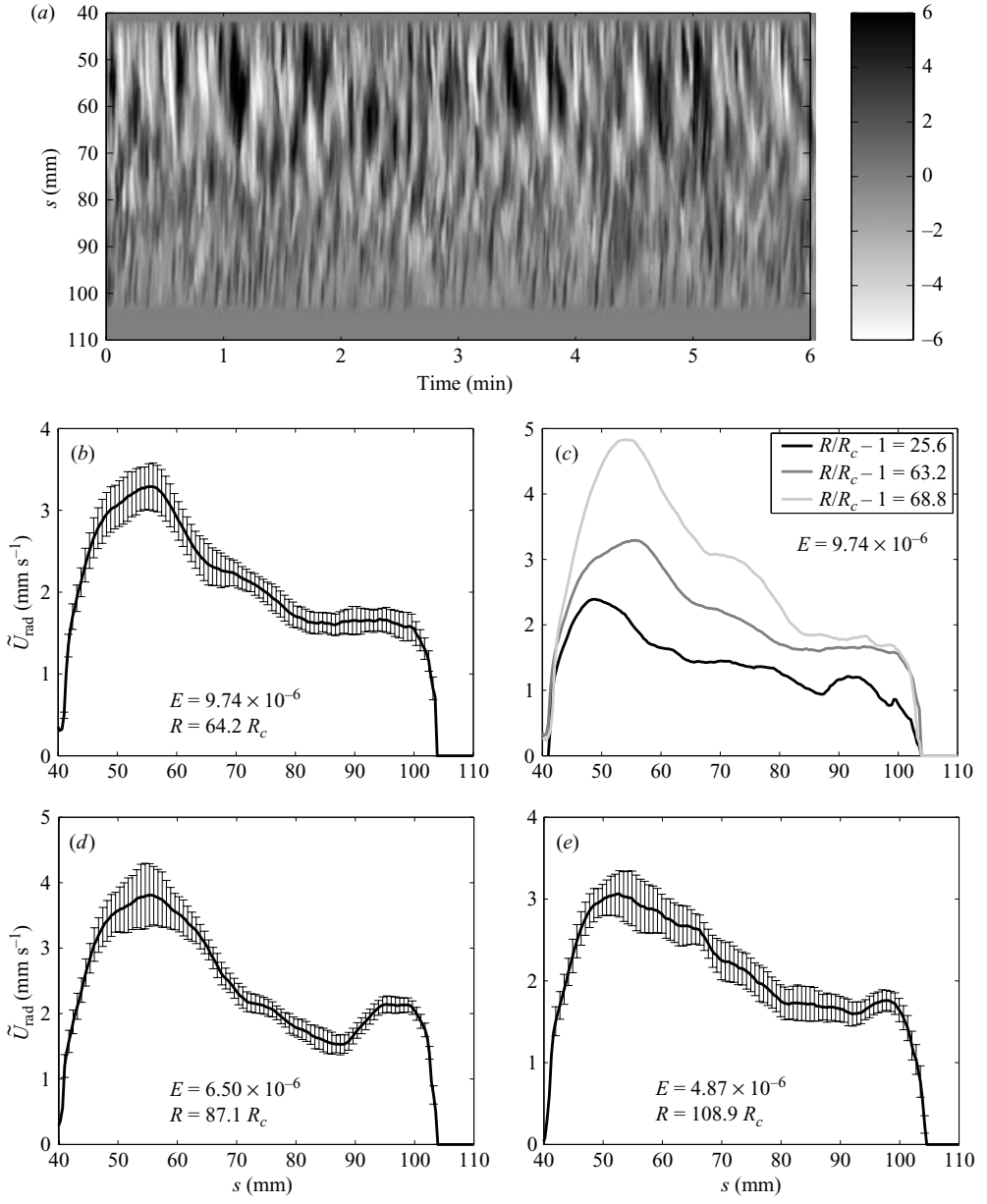

FIGURE 15. R.m.s. radial velocity profiles obtained during convection experiments performed in water ($P = 7$). (*a*) Radial velocity $u_s(s, t)$ in mm s^{-1} as a function of time and radius with $E = 9.74 \times 10^{-6}$ and $R/R_c = 64.2$. (*b–e*) r.m.s. radial velocity profiles $\widetilde{U}_{\rm rad}$ as a function of radius s for various E and R/R_c.

figure 16 compared to figure 14, the measured zonal velocity is now composed of intense zonal jets, with amplitudes ten times larger than for low values of R/R_c. This change in amplitude is presumably connected with a change in the number of jets, as indicated by the comparison between figures 14 and 16. The radial velocities (figure 15) and zonal velocities (figure 16) in this regime of supercritical convection in water are very stable in time, like the experiments performed in gallium described in § 4.1.

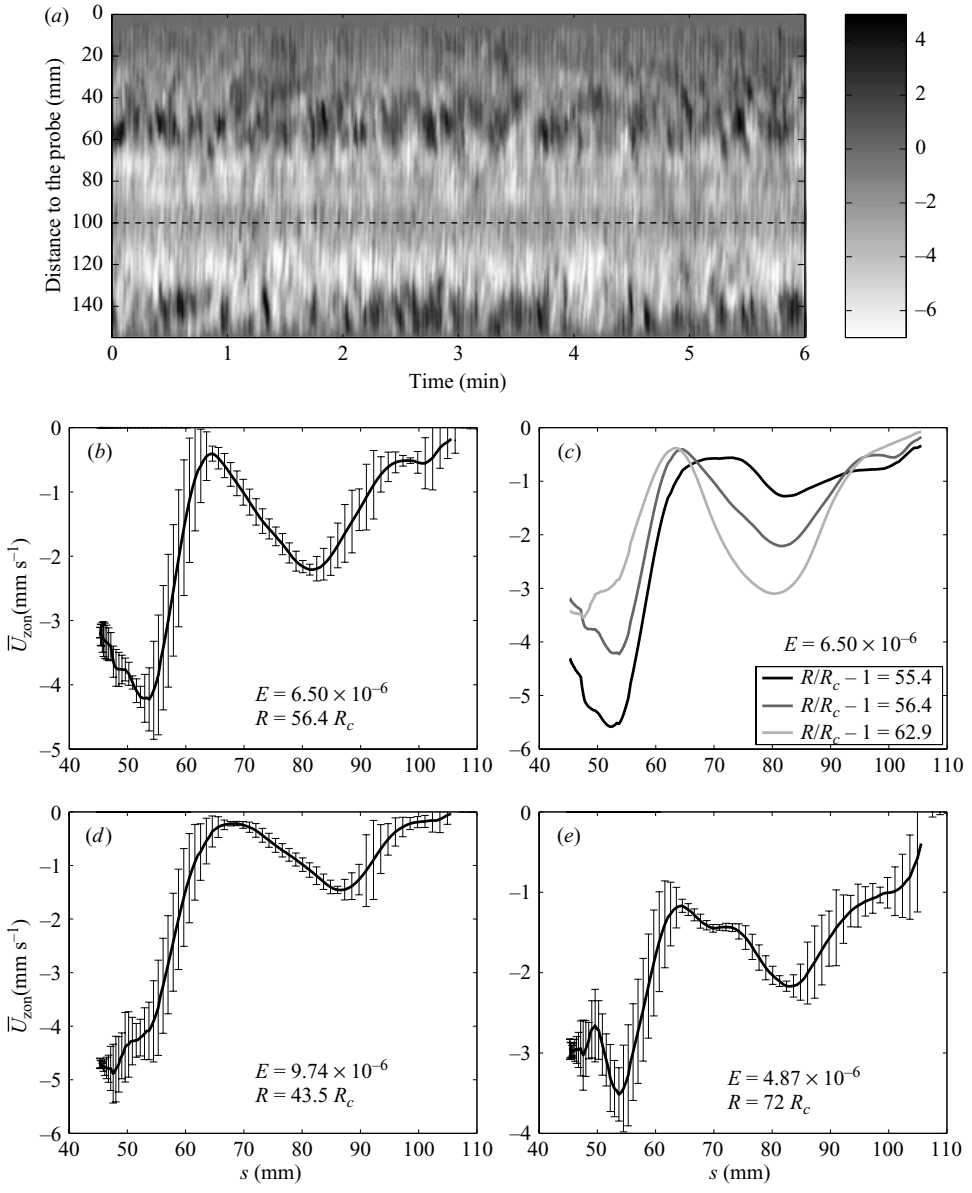

FIGURE 16. Zonal velocity profiles obtained during convection experiments performed in water ($P = 7$). (*a*) Transverse measured velocity $u_\chi(s, t)$ in mm s^{-1} as a function of time and distance to the probe, with $E = 6.50 \times 10^{-6}$, $R = 56.4\ R_c$. (*b–e*) Zonal velocity profiles $\overline{U}_{\mathrm{zon}}$ as a function of radius s for various E and R/R_c.

Also like the experiments in gallium, the size of the convective zone indicated by the radial velocities increases as a function of R/R_c (figure 15*c*). It is also important to notice that in figure 16(*c*), as the Rayleigh number increases with the Ekman number kept constant, two intense zonal retrograde jets develops (instead of one in gallium). In order to illustrate the abrupt change in the zonal velocity between the two regimes for R/R_c either smaller or larger than 40, figure 17 represents the zonal velocity $\overline{U}$

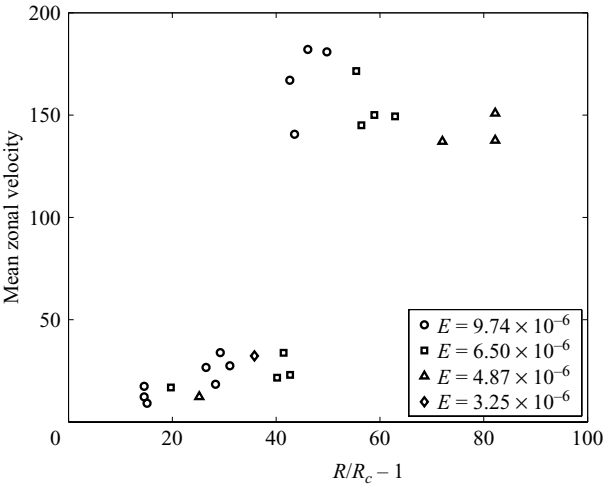

FIGURE 17. Amplitude of the mean zonal velocity $\overline{U}$ as a function of $(R/R_c - 1)$, measured from ultrasonic Doppler velocimetry in water during convection experiments, for several values of E.

(as defined in § 4.2) as a function of the forcing $(R/R_c - 1)$ for all the experiments performed in water.

5.2. *Comparison at moderate R/R_c between experiments and numerical simulations*

In the weakly nonlinear convection starting from spiral modes, numerical models have exhibited a zonal wind composed of a single retrograde jet concentrated near the tangent cylinder (Plaut & Busse 2002, 2005). By increasing the forcing up to a few times critical, the convection occurs in an area of larger and larger radius. That gives rise to multiple and unsteady jets with a short radial extent comparable with the length scale ℓ_c of the vortices at the onset of convection, as proposed by Gillet & Jones (2006).

Figure 18 shows the results of the quasi-geostrophic numerical simulation performed at a moderate R/R_c for $P = 7$ and $E = 6.50 \times 10^{-6}$. This is a typical numerical simulation at moderate R/R_c with a steady r.m.s. radial profile together with time-dependent multiple jets in the zonal direction. Ekman pumping for the modes $m \neq 0$ is crucial to obtain such multiple jets, in agreement with the suggestion by Danilov & Gurarie (2004) of a halting scale provided by friction at the boundary. Jones, Rotvig & Abdulrahman (2003) (for quasi-geostrophic-approximation simulations, rotating annulus model with finite and constant slope of the endwalls, no-slip boundary condition at the bottom surface, and stress-free boundary conditions at the cylindrical walls and at the top surface) also found that bottom friction helps to provide several jets in calculations where $\overline{\mathscr{E}} \sim \widetilde{\mathscr{E}}$. A quantitative comparison of the experiments in water at moderate forcing with the simulations shows that the quasi-geostrophic-approximation calculation reproduces fairly well both the typical shape and amplitude of the experimentally measured zonal and radial profiles of the velocity. Moreover, the time dependence and the lifetime of the experimental zonal jets are quantitatively well-reproduced numerically: as an example, figure 18 indicates that the typical time scale of the numerical zonal jets is of the same order as the time scales of the zonal jets measured experimentally in figure 14.

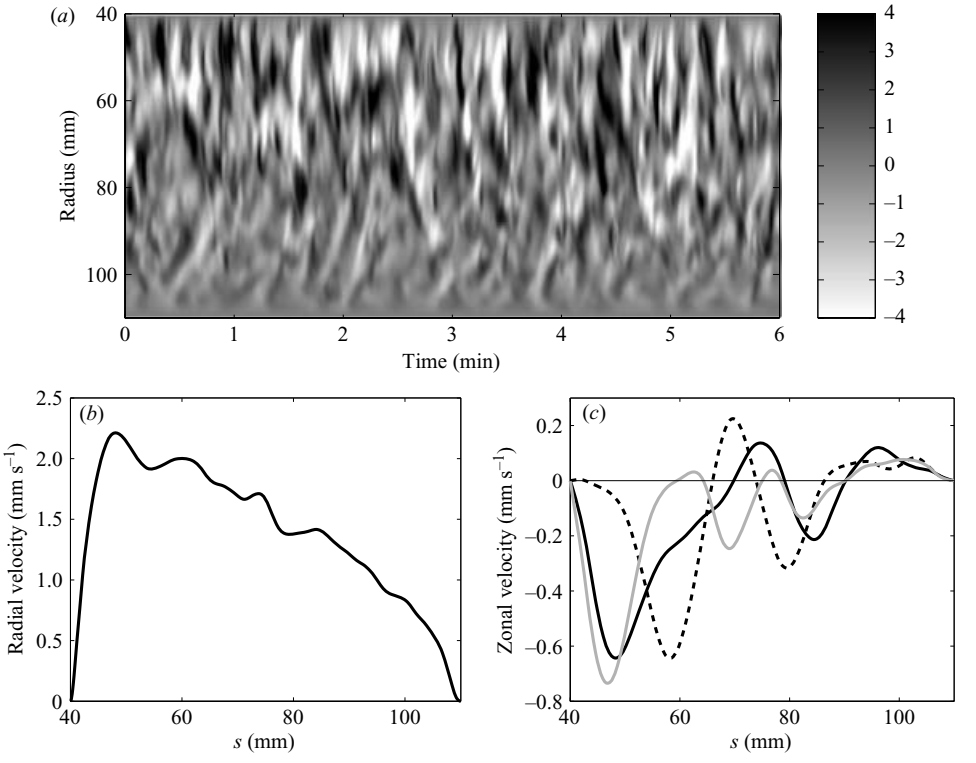

FIGURE 18. Quasi-geostrophic numerical reconstruction of velocity profiles for convection, $P = 7$, $E = 6.50 \times 10^{-6}$ and $R = 25R_c$. (*a*) R.m.s. radial velocity $u_s(s, t)$ in mm s^{-1} as a function of time and radius. (*b*) R.m.s. radial velocity profile $\widetilde{U}_{\rm rad}$ and (*c*) zonal velocity profile $\overline{U}_{\rm zon}$ extracted from the time series in (*a*). The black, dashed and grey lines are independent 50 s time averages of the mean zonal flow.

A detailed analysis of our computations (see also Gillet & Jones 2006) indicates that for $P \gg 1$, the amplitude of the zonal wind results from a balance between the volumetric viscous dissipation and the nonlinearities in equation (3.11). That equilibrium, in the case where the critical length scale dominates, leads to $\widetilde{U}^2/\ell_c \sim \overline{U}/\ell_c^2$, e.g.

$$\overline{Re}_\ell = \overline{U}\ell_c \sim {Re_\ell}^2, \tag{5.1}$$

where $Re_\ell = \widetilde{U}\ell_c$ is the local Reynolds number. Note that the jet length scale $\ell_c \sim \beta_i^{-1/3}$ that arises in our case is specific to the deep rotating convection, where barotropic thermal Rossby waves are excited (Busse 1970). In the case where $\overline{\mathscr{E}} \ll \widetilde{\mathscr{E}}$ (and at given Ekman and Prandtl numbers), a quadratic trend $\overline{U} \sim \widetilde{U}^2$ should replace the balance (4.7), previously documented in gallium. It turns out that our computations seem to follow such a quadratic law only if the convection is not too intense (namely $\widetilde{U} < O(20)$, see figure 20). This trend breaks down as multiple jets become excited. In the strong zonal flow regime, the length scale ℓ_β must be larger than ℓ_c, which gives

$$\sqrt{\frac{\overline{U}}{\beta(s)}} \geqslant \ell_c \sim \beta_i^{-1/3}. \tag{5.2}$$

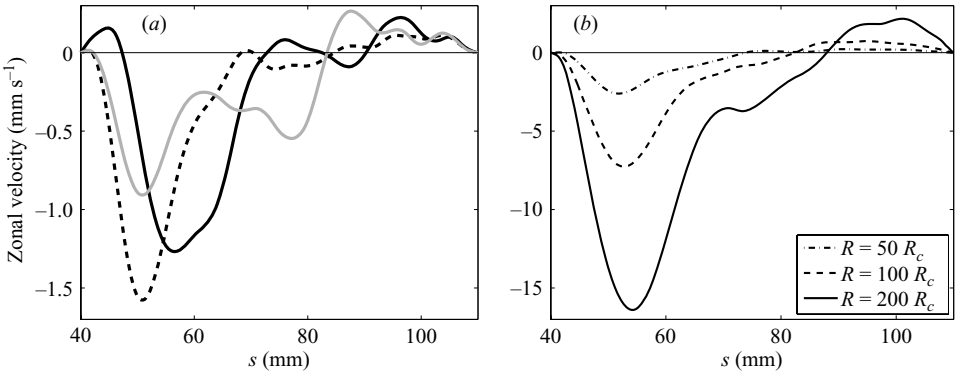

FIGURE 19. Quasi-geostrophic numerical reconstruction of velocity profiles for convection at $P = 7$ and $E = 6.50 \times 10^{-6}$. (*a*) Zonal velocity profiles $\overline{U}_{\rm zon}$ (in mm s^{-1}) for $R = 40R_c$. The black, dashed and grey lines are independent 50 s time averages of the mean zonal flow. (*b*) Zonal velocity profiles $\overline{U}_{\rm zon}$ (in mm s^{-1}) for several values of the forcing. For comparison with figure 17 the values of volumetric mean of the zonal flow for the calculations performed at $R/R_c = 50,\ 100$, and 200 are respectively $\overline{U} = 72,\ 212$ and 518.

This means that for the strong zonal flow regime to arise, the Reynolds number $\overline{U}$ must become larger than a value that evolves as $\beta(s)\beta_i^{-2/3} \sim E^{-1/3}$: the Reynolds number at the transition between weak and strong zonal flow regimes should increase with decreasing E. If the changeover in the pattern of zonal motions is always observed above $R/R_c \simeq 40$, it is not clear from our measurements whether the transition occurs at increasing values of R/R_c as E is decreased (see figure 17).

5.3. *Large-amplitude zonal winds measured in highly supercritical convection experiments*

Our experiments in water present drastically different jet amplitudes and shapes as R/R_c becomes larger than about 40 (figure 17). Such abrupt changes of the number and the amplitude of the zonal jets have not been captured numerically in our model. Our quasi-geostrophic computations show instead a rather smooth evolution of $\overline{U}$ with the forcing. Nevertheless by increasing R/R_c far enough, we have reached a parameter regime where $\overline{\mathscr{E}} \gg \widetilde{\mathscr{E}}$.

The work of Gillet & Jones (2006) based on the critical size ℓ_c also fails to explain such a behaviour. This was somewhat expected since their weakly nonlinear analysis (§ 3 of their paper) was developed for $P \to \infty$, the zonal flow vanishing. For a large (but finite) Prandtl number such as $P = 7$, if the domain of validity of their approach can (surprisingly) be extended to relatively large values of R/R_c, it is still in a parameter domain where $\overline{U}$ remains small.

Here the observed relationship between the number and amplitude of the zonal jets is in qualitative agreement with the suggestion by Rhines of a balance between inertial and Coriolis accelerations leading to an increase of the wavelength as the flow is more energetic – see the discussion of the gallium experiments and expression (4.3). Figure 16(*c*) also indicates that the zonal energy is redistributed between jets as the forcing increases: the amplitude of the jet close to the inner cylinder weakens whereas the second jet, which develops at a larger radius, strengthens as R is increased. Instead of such double jets, we obtain with our quasi-geostrophic computations at very large forcing (up to 200 times supercritical) intense jets near the tangent cylinder, as shown in figure 19(*b*). They are very similar to the ones detailed in our gallium study:

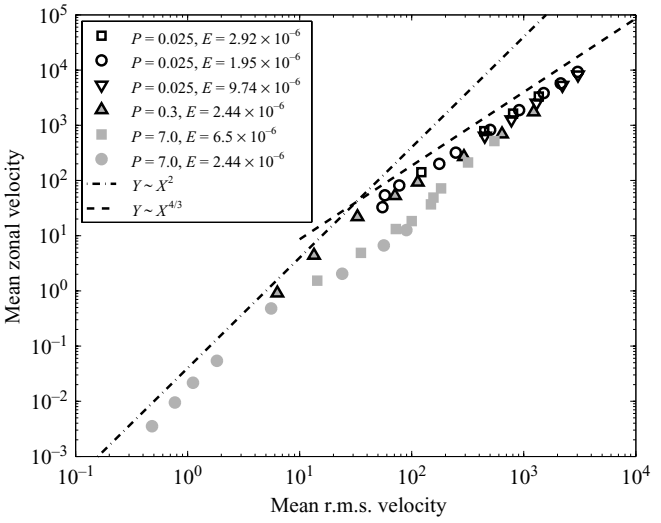

FIGURE 20. Amplitude of the mean zonal velocity $\overline{U}$ as a function of the mean r.m.s. velocity $\widetilde{U}$ from quasi-geostrophic simulations performed at various P and E. The simulations in gallium are equivalent to the ones in figure 12(*a*). The dot-dashed line is given by the quadratic evolution from equation (5.1) and the dashed line by the 4/3 scaling law from equation (4.7).

mainly concentrated near the inner cylinder and steady in time. Moreover their radial extent increases with the forcing. In between the two extreme behaviours, we obtained transitional zonal winds for $R \simeq 40R_c$ (see figure 19*a*). The sharp transition observed in the experiment between weak and strong zonal winds (figure 17) is not retrieved numerically.

As seen in figure 20, the computations for the water case show that the zonal wind departs from a quadratic law to reach the 4/3 trend. It is striking in figure 20 that the intensity of the zonal wind, once on the asymptote of slope 4/3, does not depend on the Prandtl number (three different P values have been computed from 0.025 to 7). This is characteristic of the inertial regime, where thermal diffusivity no longer plays a role and kinematic viscosity enters the scaling through the friction term only. Our experimental observations in water are indeed in qualitative agreement with the gallium analysis. As we do not observe multiple jets in gallium, we cannot see the number of jets decrease. We interpret this difference between experiments in gallium and experiments in water as a direct consequence of the smaller length scale at convection onset in water than in gallium. The width of the jets is derived from the radial length scale of convective motions, which is constructed, at the onset, from the largest diffusivity (ν in water, κ in gallium, see table 2). We would need to rotate gallium four times faster than water to compensate for the difference between their diffusivities.

Similarly, one can speculate which kind of dynamics occurs in the three-dimensional computations of the rapidly rotating spherical convection where the Reynolds number does not exceed a few hundred. In the case of no-slip boundary conditions it is difficult to generate intense zonal flows, that are damped by the boundary friction. Following our considerations of the ratio $\overline{U}/\widetilde{U}$, this means that the Rhines scenario is unlikely to happen, unless first the forcing is strong enough for the zonal flow to dominate, but also the Ekman number is small enough to avoid a loss of geostrophy. In the non-magnetic part of his three-dimensional numerical study, Aubert (2005) interprets the

zonal flow in the frame of the Rhines scenario developed by Aubert *et al.* (2001), who derived the scaling law $\overline{U} \sim (R_Q/P^2)^{4/5} E^{9/10}$, where R_Q is the heat-flux-based Rayleigh number. This law is not compatible with (4.7). First Aubert *et al.* (2001) inferred a Rhines scale based on the r.m.s. motions, instead of the zonal flow here. Second, they assumed that the increase in the length scale is negligible – in contradiction with the Rhines scenario, but see the discussion after equation (4.7). Gillet & Jones (2006) have reinstated the increase in the length scale into the scaling, and found instead $\overline{U} \sim (R_Q/P^2)^{3/5} E^{3/10}$. They observed that neither the 4/5 nor the 3/5 scalings presented above represent well the Prandtl number dependence of our computations. An explanation may be that in the computations where the Reynolds number does not exceed a few hundred, a reverse cascade does not occur.

The situation is different in the computations using stress-free boundary conditions where intense zonal jets can be generated more easily. This configuration is more suited to the atmospheres of the giant planets. For instance Heimpel, Aurnou & Wicht (2005) have been able to interpret the zonal flow width, inside the tangent cylinder, in term of the Rhines length scale including a varying β-effect. Interestingly Aurnou & Heimpel (2004), using a rigid bottom boundary, find vortex-scale unsteady zonal flows at high latitudes (inside the tangent cylinder), with values of the Reynolds number of a few hundred, that could be related to the dynamics described in Gillet & Jones (2006) (see § 5.2).

Key features recently detected in three-dimensional computations were previously discussed in quasi-geostrophic studies. This gives some credence to this approach: the transition to different dynamics in the equatorial region was pointed out by Yano, Talagrand & Drossart (2003), and Jones *et al.* (2003) stressed the role played by the bottom friction, which reduces the Rhines length scale (by decreasing the amplitude of the zonal motions) and therefore allows for the existence of multiple jets.

6. Discussion

We have explored thermal convection in a rapidly rotating sphere ($E \sim 10^{-6}$), with an experiment backed by a quasi-geostrophic numerical simulation. We have compared the experimental and numerical approaches at both low and large Prandtl numbers. At the onset of convection, the accuracy of the estimation of the critical parameters from the quasi-geostrophic approximation model is improved when the Ekman pumping is taken into account for the non-axisymmetric modes. In the nonlinear case, the impossibility of describing thermal boundary layers attached to the outer sphere surface in the frame of the quasi-geostrophic approximation implies that our model fails to reproduce the amplitude of convection as a function of R/R_c. It does however reproduce the observed relationships between convective motions, with a radial component, and zonal motions.

At $P = 0.025$ (gallium), the zonal flow – mainly a single retrograde jet – makes up most of the kinetic energy in our experiment even for a slightly supercritical temperature difference between the inner body and outer sphere. That has enabled us to derive the relation $\overline{U} \sim \widetilde{U}^{4/3}$ between the amplitudes of radial and zonal motions in the frame of the β-plane turbulence – see equation (4.7). This scaling law is in excellent agreement with both our experimental measurements and our numerical simulations. According to this approach, the typical lateral extent of the jet should increase with the convective forcing. We could not substantiate this behaviour in gallium because the jet already occupies a large fraction of the shell radius, and sphericity effects become dominant. However, a faint prograde equatorial jet appears

next to the strong retrograde inner jet when the Ekman number is not too small ($E \geqslant 2 \times 10^{-6}$).

At $P = 7$ (water) we have been able to study convection for R/R_c up to 80. At low forcing, the weakly nonlinear theory predicts a single retrograde jet again. We could not access this regime experimentally but quasi-geostrophic simulations reproduce well this behaviour. At intermediate forcings ($R/R_c < 40$), our experiments reveal a new regime with unsteady multiple jets (alternatively prograde and retrograde with radial wavenumber up to four, see figure 16), as discovered by Jones *et al.* (2003) in a quasi-geostrophic simulation. Like them and in agreement with Danilov & Gurarie (2004), we note that bottom friction for both the azimuthal and the non-azimuthal motions is essential for obtaining this regime. The zonal kinetic energy remains small in this regime and the radial extent of each jet is not very different from that of a single jet at lower forcing. We reproduce the sequence from a single jet to multiple zonal jets with our numerical simulations, showing similar zonal flow amplitudes, time dependence, and shapes. It suggests that the scaling laws developed by Gillet & Jones (2006) in the case where the zonal wind is weaker than the convective flow, based on numerical simulations, are supported by our velocity measurements. For very large forcings ($R/R_c > 40$), our velocity measurements indicate intense retrograde jets, stable in time, with a large radial extent (twice as large and up to ten times more intense than the jets obtained at lower forcings). As in gallium, we have associated this feature with an inverse cascade, including the emergence of the Rhines scale as the zonal motions become more intense than the non-axisymmetric ones. In agreement with Rhines' theory, the general trend is for the lateral extent of the jets to increase with the convective forcing. However, this tendency is tempered by the strong variation of β with s, due to the curvature of the spherical shell, and by the finite size of the convective vortices. Manneville & Olson (1996) even inferred the opposite trend from laboratory experiments in water at higher Ekman number ($E = 4 \times 10^{-5}$) and in a spherical shell that was less deep. The relationships between the number of jets, the zonal wind amplitude and the rotation rate require a more systematic experimental study.

Concerning the relationship between the zonal and r.m.s. velocities, we find a transition for $\overline{U}$ from a $\widetilde{U}^2$ to a $\widetilde{U}^{4/3}$ power law (see figure 20). The quadratic law at small forcing reflects the quadratic nature of the Reynolds stress, which is the source of the azimuthal motion, when the fluctuations in radial velocity and the gradient of zonal velocity are perfectly correlated, if the characteristic size does not change. The $\widetilde{U}^{4/3}$ law is obtained when the increase of the size ℓ_β with $\widetilde{U}$ is taken into account. This contrasts with the interpretation of Christensen (2002) who also observed such a transition in three-dimensional convection models, with stress-free boundary conditions, at larger Ekman numbers and explained it in terms of a loss of geostrophy, leading to decorrelation between the two velocities – see also the early work by Gilman (1978*b*). Since our numerical simulations are quasi-geostrophic, this effect is not present in our case. As expected from Rhines' theory, the transition occurs when the zonal kinetic energy dominates. Our interpretation points to a universal behaviour at high Rayleigh number whatever the Prandtl number. This is obscured in our experiments by the large size of convective cells in gallium at the onset.

We find a very good agreement between our experimental velocity profiles and our quasi-geostrophic simulations, but we also observe a few differences. In the gallium experiments, convection extends farther toward the equator and displays less prograde tilt than predicted. In the water experiments, the strong retrograde jets observed at large forcings could not be reproduced numerically. Both effects could be due to

the three dimensional nature of the temperature field, since the evolution of the temperature variations along the rotation axis and the latitudinal distribution of the heat flux cannot be described in the frame of the quasi-geostrophic approximation.

The zonal flow in the numerical dynamos using no-slip boundary conditions follows different physics dominated by thermal wind (Aubert 2005). But the comparison between the numerical dynamos and the planetary cores only holds for the long time-scale features, because of the limits in the parameter domain. On the contrary, the experimental and numerical models that we have developed cast light on some features of Earth's core dynamics at time scales from one year to a few hundreds years. It will require not only lower Ekman and magnetic Prandtl numbers, but also larger forcings to catch such features in three-dimensional numerical dynamos. The dynamics of rapid motions that are inferred from magnetic observations and that thus have periods small compared to the magnetic diffusion time (10^4 years for the Earth's core) are not yet well understood. We envision that rotation forces provide the main constraint on these diffusionless rapid motions, since inertial waves, which arise in the presence of rotation, have much shorter periods that Alfvén waves, which arise in the presence of a magnetic field. Rapidly rotating convection studies can thus guide us in our understanding of the Earth's core dynamics on centennial time scales. There is however a specific action of the magnetic field, on zonal motions only, for short time scales (10–100 years), as the time evolution of geostrophic motions follows an equation of the Alfvén wave type. An unanswered question is what mechanism sets off these geostrophic motions, which are detected in the Earth's core through the observed magnetic field (Dumberry & Bloxham 2003). The dynamo simulation of Takahashi, Matsushima & Honkura (2005) has illustrated the part that the inertial term $(\boldsymbol{u}\cdot\nabla)\boldsymbol{u}$ can play in the acceleration of geostrophic motions. This also motivates studies on the emergence of zonal motions from Rossby waves in deep spherical shells such as the present work. In this context we present in a companion paper (Gillet *et al.* 2007) our work on rapidly rotating spherical convection in the presence of an imposed magnetic field.

We are indebted to Philippe Cardin and Julien Aubert who developed the original quasi-geostrophic code, and largely contributed to the experimental set-up. We thank Jean-Paul Masson and Robert Bolcato for their skilled technical assistance and Chris Jones for discussion and helpful comments. N.G. is grateful to *École Doctorale "Terre, Univers et Environnement"* and Université Joseph Fourier (Grenoble) for the award of a studentship. This work was supported by the program Expérimentation of CNRS/INSU. The computations were performed on the *Service Commun de Calcul Intensif de l'Observatoire de Grenoble*.

REFERENCES

Ardes, M., Busse, F. H. & Wicht, J. 1997 Thermal convection in rotating spherical shells. *Phys. Earth Planet. Inter.* **99**, 55–67.

Aubert, J. 2005 Steady zonal flows in spherical shell fluid dynamos. *J. Fluid Mech.* **542**, 53–67.

Aubert, J., Brito, D., Nataf, H.-C., Cardin, P. & Masson, J. 2001 A systematic experimental study of rapidly rotating spherical convection in water and liquid gallium. *Phys. Earth Planet. Inter.* **128**, 51–74.

Aubert, J., Gillet, N. & Cardin, P. 2003 Quasigeostrophic models of convection in rotating spherical shells. *Geochem. Geophys. Geosys.* **4(7)**, 1052.

Aubert, J., Jung, S. & Swinney, H. 2002 Observations of zonal flows created by potential vorticity mixing in a rotating fluid. *Geophys. Res. Lett.* **9**, 1876–1879.

Aurnou, J. M. & Heimpel, M. 2004 Zonal jets in rotating convection with mixed mechanical boundary conditions. *Icarus* **169**, 492–498.

Aurnou, J. M. & Olson, P. L. 2001 Strong zonal winds in the major planets. *Geophys. Res. Lett.* **28**, 153–174.

Brito, D. 1998 Approches expérimentales et théoriques de la dynamique du noyau terrestre. PhD thesis, Université Paris VII.

Brito, D., Nataf, H.-C., Cardin, P., Aubert, J. & Masson, J. 2001 Ultrasonic Doppler velocimetry in liquid gallium. *Exps. Fluids* **31**, 653–663.

Busse, F. 1970 Thermal instabilities in rapidly rotating systems. *J. Fluid Mech.* **44**, 441–460.

Busse, F. 1986 Asymptotic theory of convection in a rotating, cylindrical annulus. *J. Fluid Mech.* **173**, 545–556.

Busse, F. & Carrigan, C. 1976 Convection induced by centrifugal buoyancy. *J. Fluid Mech.* **62**, 579–592.

Busse, F. & Or, A. C. 1986 Convection in a rotating cylindrical annulus. Part 1. Thermal Rossby waves. *J. Fluid Mech.* **166**, 173–187.

Cardin, P. & Olson, P. 1992 An experimental approach to thermochemical convection in the Earth's core. *Geophys. Res. Lett.* **19**, 1995–1998.

Cardin, P. & Olson, P. 1994 Chaotic thermal convection in a rapidly rotating spherical shell: consequences for flow in the outer core. *Phys. Earth Planet. Inter.* **82**, 235–239.

Carrigan, C. R. & Busse, F. H. 1983 An experimental and theoretical investigation of the onset of convection in rotating spherical shells. *J. Fluid Mech.* **126**, 287–305.

Chamberlain, J. A. & Carrigan, C. R. 1986 An experimental investigation of convection in a rotating sphere subject to time varying thermal boundary conditions. *Geophys. Astrophys. Fluid Dyn.* **35**, 303–327.

Chen, C. X. & Zhang, K. 2002 Nonlinear convection in a rotating annulus with a finite gap. *Geophys. Astrophys. Fluid Dyn.* **96**, 499–518.

Christensen, U. R. 2001 Zonal flow driven by deep convection in the major planets. *Geophys. Res. Lett.* **13**, 2553–2556.

Christensen, U. R. 2002 Zonal flow driven by strongly supercritical convection in rotating spherical shells. *J. Fluid Mech.* **470**, 115–133.

Christensen, U. R. & Tilgner, A. 2004 Power requirement of the geodynamo from ohmic losses in numerical and laboratory dynamos. *Nature* **429**, 169–171.

Cordero, S. & Busse, F. H. 1992 Experiments on convection in rotating hemispherical shells – Transition to a quasi-periodic state. *Geophys. Res. Lett.* **19**, 733–736.

Danilov, S. & Gurarie, D. 2002 Rhines scale and spectra of the β-plane turbulence with bottom drag. *Phys. Rev.* E **65**, 067301.

Danilov, S. & Gurarie, D. 2004 Scaling, spectra and zonal jets in beta-plane turbulence. *Phys. Fluids* **16**, 2592–2602.

De Wijs, G., Kresse, G., Vocadlo, L., Dobson, D., Alfè, D., Gillan, M. J. & Price, G. D. 1998 The viscosity of liquid iron at the physical conditions of the Earth's core. *Nature* **392**, 805–807.

Dormy, E., Soward, A. M., Jones, C. A., Jault, D. & Cardin, P. 2004 The onset of thermal convection in rotating spherical shells. *J. Fluid Mech.* **501**, 43–70.

Dormy, E., Valet, J.-P. & Courtillot, V. 2000 Numerical models of the geodynamo and observational constraints. *Geochem. Geophys. Geosys.* **1**, 62.

Dumberry, M. & Bloxham, J. 2003 Torque balance, Taylor's constraint and torsional oscillations in a numerical model of the geodynamo. *Phys. Earth Planet. Inter.* **140**, 29–51.

Gailitis, A., Lielausis, O., Dement'ev, S., Platacis, E., Cifersons, A., Gerbeth, G., Gundrum, T., Stefani, F., Christen, M., Hänel, H. & Will, G. 2000 Detection of a flow induced magnetic field eigenmode in the Riga dynamo facility. *Phys. Rev. Lett.* **84**, 4365–4368.

Galperin, B., Nakano, H., Huang, H.-P. & Sukoriansky, S. 2004 The ubiquitous zonal jets in the atmospheres of giant planets and Earth's ocean. *Geophys. Res. Lett.* **31**, L13303.

Gillet, N. 2004 Magnéto-convection dans une sphère en rotation rapide: approches experimentale et numérique de la convection dans les noyaux planetaires. PhD thesis, Université Joseph-Fourier (Grenoble I).

Gillet, N., Brito, D., Jault, D. & Nataf, H.-C. 2007 Experimental and numerical studies of magnetoconvection in a rapidly rotating spherical shell. *J. Fluid Mech.* **580**, 123–143.

Gillet, N. & Jones, C. A. 2006 The quasi-geostrophic model for rapidly rotating spherical convection outside the tangent cylinder. *J. Fluid Mech.* **554**, 343–369.

Gilman, P. A. 1977 Nonlinear dynamics of Boussinesq convection in a deep rotating spherical shell–I. *Geophys. Astrophys. Fluid Dyn.* **8**, 93–135.

Gilman, P. A. 1978*a* Nonlinear dynamics of Boussinesq convection in a deep rotating spherical shell–II: effect of temperature boundary conditions. *Geophys. Astrophys. Fluid Dyn.* **11**, 157–179.

Gilman, P. A. 1978*b* Nonlinear dynamics of Boussinesq convection in a deep rotating spherical shell–III: effect of velocity boundary conditions. *Geophys. Astrophys. Fluid Dyn.* **11**, 181–203.

Greenspan, H. P. 1968 *The Theory of Rotating Fluids*. Cambridge University Press.

Heimpel, M., Aurnou, J. & Wicht, J. 2005 Simulation of equatorial and high-latitude jets on Jupiter in a deep convection model. *Nature* **438**, 193–196.

Herrmann, J. & Busse, F. H. 1997 Convection in a rotating cylindrical annulus. Part 4. Modulations and transition to chaos at low Prandtl numbers. *J. Fluid Mech.* **350**, 209–229.

Hide, R. & James, I. N. 1983 Differential rotation produced by potential vorticity mixing in a rapidly rotating fluid. *Geophys. J. R. Astron. Soc.* **74**, 301–312.

Hide, R., Lewis, S. R. & Read, P. L. 1994 Sloping convection: a paradigm for large-scale waves and eddies in planetary atmospheres? *Chaos* **4**, 135–162.

Hide, R. & Mason, P. J. 1970 Baroclinic waves in a rotating fluid subject to internal heating. *Phil. Trans. R. Soc. Lond.* A **268**, 201–232.

Hulot, G., Eymin, C., Langlais, B., Mandea, M. & Olsen, N. 2002 Small scale structure of the geodynamo inferred from Oersted and Magsat satellite data. *Nature* **416**, 620–623.

Ingersoll, A., Beebe, R. F., Mitchell, J. L., Garneau, G. W., Yagi, G. M. & Müller, J.-P. 1981 Interaction of eddies and mean zonal flow on Jupiter as inferred from Voyager 1 and 2 images. *J. Geophys. Res.* **86**, 8733–8743.

Ingersoll, A. & Pollard, D. 1982 Motions in the interiors and atmospheres of Jupiter and Saturn: scale analysis, anelastic equations, barotropic stability criterion. *Icarus* **52**, 62–80.

Jackson, A. 2003 Intense equatorial flux spots on the surface of the Earth's core. *Nature* **424**, 760–763.

Jones, C. A. 2003 Dynamos in planets. In *Stellar Astrophysical Fluid Dynamics* (ed. M. J. Thompson & J. Christensen-Dalsgaard). Cambridge University Press.

Jones, C. A., Rotvig, J. & Abdulrahman, A. 2003 Multiple jets and zonal flows on jupiter. *Geophys. Res. Lett.* **30**, 1731.

Jones, C. A., Soward, A. N. & Mussa, A. I. 2000 The onset of convection in a rapidly rotating sphere. *J. Fluid Mech.* **405**, 157–179.

Kono, M. & Roberts, P. H. 2002 Recent geodynamo simulations and observations of the geomagnetic field. *Rev. Geophys.* **40**, 1013.

Manin, D. 1990 Characteristic size of vortices in developped quasi-two-dimensional flows. *Izv. Akad. Nauk. SSSR, Atmos. Ocean. Phys.* **26(6)**, 426–429.

Manneville, J. & Olson, P. 1996 Banded convection in rotating fluid spheres and the circulation of the Jovian atmosphere. *Icarus* **122**, 242–250.

Morin, V. & Dormy, E. 2004 Time dependent β-convection in rapidly rotating spherical shell. *Phys. Fluids* **16**, 1603–1609.

Or, A. C. & Busse, F. 1987 Convection in a rotating cylindrical annulus. Part 2. Transitions to asymmetric and vacillating flow. *J. Fluid Mech.* **174**, 313–326.

Plaut, E. & Busse, F. 2002 Low prandtl number convection in a rotating cylindrical annulus. *J. Fluid Mech.* **464**, 345–363.

Plaut, E. & Busse, F. 2005 Multicellular convection in rotating annuli. *J. Fluid Mech.* **528**, 119–133.

Read, P. L. 1986 Regimes of axisymmetric flow in an internally heated rotating fluid. *J. Fluid Mech.* **168**, 225–289.

Read, P. L., Lewis, S. R. & Hide, R. 1997 Laboratory and numerical studies of baroclinic waves in an internally heated rotating fluid annulus: a case of wave/vortex duality? *J. Fluid Mech.* **337**, 155–191.

Read, P. L., Yamazaki, Y. H., Lewis, S. R., Williams, P. D., Miki-Yamazaki, K., Sommeria, J., Didelle, H. & Fincham, A. 2004 Jupiter's and Saturn's convectively driven banded jets in the laboratory. *Geophys. Res. Lett.* **31**, L22701.

Rhines, P. B. 1975 Wave and turbulence on a beta-plane. *J. Fluid Mech.* **122**, 417–443.

Rhines, P. B. & Young, W. 1982 Homogeneization of potential vorticity in planetary gyres. *J. Fluid Mech.* **122**, 347–367.

Roberts, P. H. 1968 On the thermal instability of a self-graviting fluid sphere containing heat sources. *Phil. Trans. R. Soc. Lond.* A **263**, 93–117.

Schaeffer, N. & Cardin, P. 2005 Quasi-geostrophic model of the instabilities of the stewartson layer in flat and depth varying containers. *Phys. Fluids* **17**, 104111.

Schnaubelt, M. & Busse, F. H. 1992 Convection in a rotating cylindrical annulus. Part 3. Vacillating and spatially modulated flows. *J. Fluid Mech.* **245**, 155–173.

Secco, R. A. & Schloessin, H. H. 1989 The electrical resistivity of solid and liquid Fe at pressures up to 7 GPa. *J. Geophys. Res.* **94**, 5887–5894.

Shew, W. & Lathrop, D. P. 2005 Liquid sodium model of geophysical core convection. *Phys. Earth Planet. Inter.* **153**, 136–149.

Starchenko, S. & Jones, C. 2002 Typical velocities and magnetic field strengths in planetary interiors. *Icarus* **157**, 426–435.

Stewartson, K. 1966 On almost rigid rotation. Part 2. *J. Fluid Mech.* **26**, 131–144.

Stieglitz, R. & Müller, U. 2001 Experimental demonstration of a homogeneous two-scale dynamo. *Phys. Fluids* **13**, 561–564.

Sumita, I. & Olson, P. 2000 Laboratory experiments on high rayleigh number thermal convection in a rapidly rotating hemispherical shell. *Phys. Earth Planet. Inter.* **117**, 153–170.

Sumita, I. & Olson, P. 2003 Experiments on highly supercritical thermal convection in a rapidly rotating hemispherical shell. *J. Fluid Mech.* **492**, 271–287.

Takahashi, F., Matsushima, M. & Honkura, Y. 2005 Simulations of a quasi-Taylor state geomagnetic field including polarity reversals on the earth simulator. *Science* **309**, 459–461.

Tilgner, A. & Busse, F. H. 1997 Finite amplitude convection in rotating spherical fluid shells. *J. Fluid Mech.* **332**, 359–376.

Van de Konijnenberg, J. A., Nielsen, A. H., Rasmussen, J. J. & Stenum, B. 1998 Shear-flow instability in a rotating fluid. *J. Fluid Mech.* **387**, 177–204.

Williams, G. 1978 Planetary circulations: 1. Barotropic representation of jovian and terrstrial turbulence. *J. Atmos. Sci.* **35**, 1399–1426.

Yano, J., Talagrand, O. & Drossart, P. 2003 Outer planets: Origins of atmospheric zonal winds. *Nature* **421**, 36.

Yano, J.-I. 1992 Asymptotic theory of thermal convection in rapidly rotating systems. *J. Fluid Mech.* **236**, 535–556.

Zhang, K. 1992*a* On inertial waves in the earth's fluid core. *Geophys. Res. Lett.* **19**, 737–740.

Zhang, K. 1992*b* Spiralling columnar convection in rapidly rotating spherical fluid shell. *J. Fluid Mech.* **236**, 535–556.

Zhang, K. 1993 On equatorially trapped boundary inertial waves. *J. Fluid Mech.* **248**, 203–217.

Zhang, K. & Busse, F. H. 1987 On the onset of convection in rotating spherical shells. *Geophys. Astrophys. Fluid Dyn.* **39**, 119–147.

Zhang, K. & Jones, C. A. 1992 The influence of Ekman boundary layers on rotating convection. *Geophys. Astrophys. Fluid Dyn.* **71**, 145–162.